IDŐJÁRÁS

QUARTERLY JOURNAL
OF THE HUNGARIAN METEOROLOGICAL SERVICE

CONTENTS

****

http://omsz.met.hu/english/ref/jurido/jurido_en.html

VOL. 108 * NO. 4 * OCTOBER – DECEMBER 2004

IDŐJÁRÁS

Quarterly Journal of the Hungarian Meteorological Service

Editorial Office: P.O. Box 39, H-1675 Budapest, Hungary or
Gilice tér 39, H-1181 Budapest, Hungary
E-mail: bozo.l@met.hu or *antal.e@met.hu*
Fax: (36-1) 346-4809

Subscription by

mail: IDŐJÁRÁS, P.O. Box 39, H-1675 Budapest, Hungary;
E-mail: bozo.l@met.hu or *antal.e@met.hu*; *Fax: (36-1) 346-4809*

IDŐJÁRÁS

Quarterly Journal of the Hungarian Meteorological Service
Vol. 108, No. 4, October–December 2004, pp. 209–251

The greenhouse effect and the spectral decomposition of the clear-sky terrestrial radiation

Ferenc M. Miskolczi[*1] and **Martin G. Mlynczak**[2]

[1]*Analytical Services & Materials Inc.,*
One Enterprise Parkway, Suite 300 Hampton, VA 23666, U.S.A.
E-mail: f.m.miskolczi@larc.nasa.gov

[2]*NASA Langley Research Center, Mail Stop 420, Hampton, VA 23681-2199, U.S.A.*
E-mail: m.g.mlynczak@larc.nasa.gov

(Manuscript received March 8, 2004; in final form November 1, 2004)

Abstract—In this paper the clear-sky infrared radiation field of the Earth-atmosphere system is characterized by the spectral decomposition of the simulated upward and downward flux density components into three distinct wave number regions. The relative contributions of the far infrared, middle infrared, and windows spectral regions to the total longwave flux densities have been established. The approximate qualitative description of the meridional distributions of the zonal averages gave us a detailed insight into the role of the less explored far infrared spectral region. We demonstrate that on a global scale, the far infrared contribution to the clear-sky normalized greenhouse factor is significantly increasing toward the polar regions. Accurate computation of the transmitted and re-emitted part of the outgoing longwave radiation showed that in the far infrared the normalized upward atmospheric emittance increases poleward. This phenomenon is the direct consequence of the downward shift of the peak of the weighting functions in the strongly absorbing opaque spectral regions. The clear-sky total longwave terrestrial flux transmittance seems to be well correlated with the far infrared flux transmittance, which implies the possibility of inferring total longwave flux densities solely from far infrared observations. The zonal averages of the total normalized atmospheric upward emittances are almost independent of the water vapor column amount, they have no meridional variation, and they are constantly about fifty percent of the surface upward flux density, an indication, that the gray atmosphere in the IR is in radiative equilibrium. The meridional distribution of the greenhouse temperature change and its dependence on the atmospheric water vapor content were also evaluated. Solving the Schwarzschild-Milne equations for the bounded atmosphere the infrared atmospheric transfer and greenhouse functions were derived. The theoretically predicted greenhouse effect in the clear atmosphere are in perfect agreement with simulation results and measurements.

Key-words: greenhouse effect, radiative equilibrium, far infrared.

* Corresponding author

1. Introduction

Terrestrial radiation or outgoing longwave radiation (*OLR*) are terms which refer to the emitted infrared (IR) radiation field of the Earth-atmosphere system. An accurate knowledge of the spatial and temporal distribution of this radiation field is fundamental in climate research. When long-term radiative equilibrium between the solar and terrestrial radiation exists monitoring the *OLR* one can identify the changes in the shortwave net input into the Earth-atmosphere system. From the satellite observation of the Earth's radiation budget (*ERBE*, 2004) we estimated that the five years average effective planetary temperature is about 253.8 K. When using the observed albedo and a solar constant of 1365 W m^{-2}, this results in an effective temperature of 253.0 K. Despite the fact that the average net radiation is off by about 5 W m^{-2}, these results support the idea of the long-term radiative equilibrium.

The knowledge of the spectral characteristic of the *OLR* is equally important. Keeping the *OLR* constant, climate change might occur by changing the concentration of the greenhouse gases. Any change in the longwave atmospheric transparency will alter the contribution of the different spectral intervals to the *OLR*. For example, increased spectral *OLR* in the window regions coupled with constant total *OLR* and surface emissivity will point to an amplified greenhouse effect due to increased greenhouse gas concentration.

In principle, the classification of the spectral intervals of the terrestrial radiation must be based on observations of the spectral characteristics of the *OLR* or the downward atmospheric emittance (E_D). So far the spectral boundaries of the far infrared (FIR), middle infrared (MIR), and windows (WIN) spectral regions are not exactly defined and there is no convention accepted by the scientific community regarding these boundaries. This is primarily because in the highly variable atmosphere, the exact wavelength of the complete absorption is changing. Sometimes, due to technical or engineering constraints, the spectral sensitivity of a detector or instrument design sets the spectral boundaries. However, focusing on the spectral aspects of the Earth's radiation budget or climate change, such definitions sooner or later will be necessary. Until then, meaningful quantitative comparisons of FIR, MIR, and WIN flux densities, cooling rates, greenhouse factors, or other spectrally resolved quantities from different authors will be difficult.

On a purely physical basis, one may set the FIR upper wave number limit before or after the CO_2 15 μ fundamental absorption band. Although the separate treatment of the 15 μ CO_2 band, (620–720 cm^{-1}), is popular in broad band spectral radiative transfer models, to emphasize that the atmosphere is mostly opaque in the 1–720 cm^{-1} spectral region, in this work we have adopted the next definitions: total: 1–3000 cm^{-1}; FIR: 1–720 cm^{-1}; WIN: 720–1260 cm^{-1}; MIR: 1260–3000 cm^{-1}.

As a reference, in *Fig. 1* the positions of the FIR, WIN, and MIR spectral regions are presented together with the spectral *OLR* which was computed with 1 cm^{-1} spectral resolution for the USST 76 atmosphere. The surface upward radiation (S_U) as the blackbody emittance of the surface is also shown. In *Table 1* the numerical values of the integrated totals and averages are displayed. The first section of the table contains the quantities obtained directly from a line-by-line (LBL) simulation. The second section of the table contains some definitions of the derived quantities, and in the third part the commonly used greenhouse parameters are summarized.

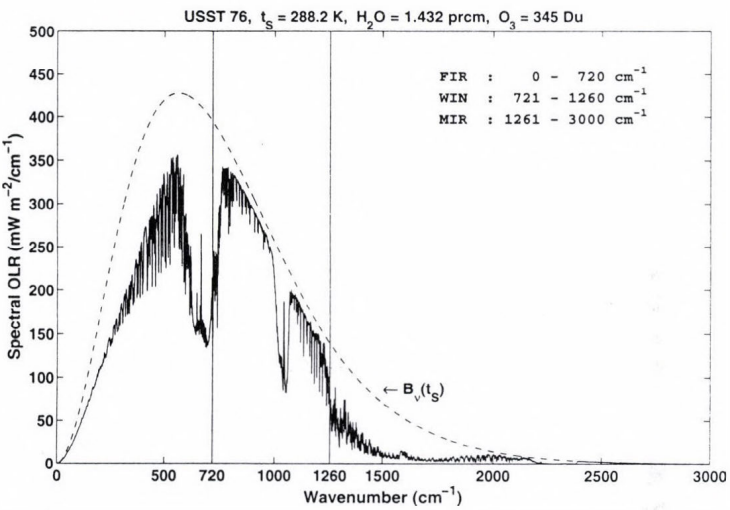

Fig. 1. Spectral *OLR* and $S_U = B_\nu(t_S)$, computed for the USST 76 atmosphere. The FIR spectral range contains the whole 15 μ CO_2 band.

In *Fig. 2* we present the basic flux density components of our simplified Earth-atmosphere radiative transfer model. As it is evident in our scheme, the shortwave atmospheric absorption and scattering together with all reflection related processes (both shortwave and longwave) are ignored.

We performed some test calculations using the tropical and subarctic winter standard atmospheres and the definitions of spectral boundaries given above. The total greenhouse forcing (G), as the difference of the S_U and *OLR* fluxes, are compared to similar results by *Brindley* and *Harries* (1997). The numerical values are summarized in *Table 2*. The large differences between the two computations are very unusual, considering, that the atmospheric profiles were fixed. The explanation is the use of different definitions for the FIR spectral limits. The dependence of the greenhouse forcing on the

wavenumber for the tropical and subarctic winter atmospheres are presented in *Fig. 3*. This figure clearly indicates the necessity of the exact definition of FIR spectral boundaries in FIR related publications. Notice the relatively large differences caused mainly by the differences in the H_2O profiles.

Table 1. Flux density components computed for the USST 76 atmosphere (W m^{-2})

	Components	Spectral intervals			
		Total	**FIR**	**MIR**	**WIN**
1	Surface upward radiation, S_U	391.2	203.1	45.9	142.2
2	Downward atmospheric emittance, E_D	290.1	199.9	42.5	47.6
3	Upward atmospheric emittance, E_U	168.9	121.2	11.3	36.3
4	Atmospheric flux transmittance, $Tr_A=1-A$	0.2162	0.0064	0.0392	0.573
5	Transmitted radiation, $S_T=S_U*Tr_A$	84.6	1.3	1.8	81.5
6	Outgoing longwave radiation, $OLR=S_T+E_U$	253.5	122.5	13.1	117.8
7	Absorbed radiation, $A_A=S_U-S_T$	306.6	201.8	44.0	60.8
8	Net atmosphere, $N_A=S_U-E_D-OLR$	-152.4	-119.3	-9.7	-23.2
9	Net surface, $N_S=E_D-S_U$	-101.1	-3.2	-3.3	-94.6
10	Terrestrial flux transmittance, $Tr_T=OLR/S_U$	0.648	0.603	0.285	0.828
11	Greenhouse factor, $G=S_U-OLR$	137.7	80.6	32.8	24.4
12	Normalized greenhouse factor, $G_N=1-Tr_T$	0.352	0.397	0.715	0.172
13	Inverse Tr_T, $I_T=1/Tr_T$	1.54	1.658	3.509	1.208

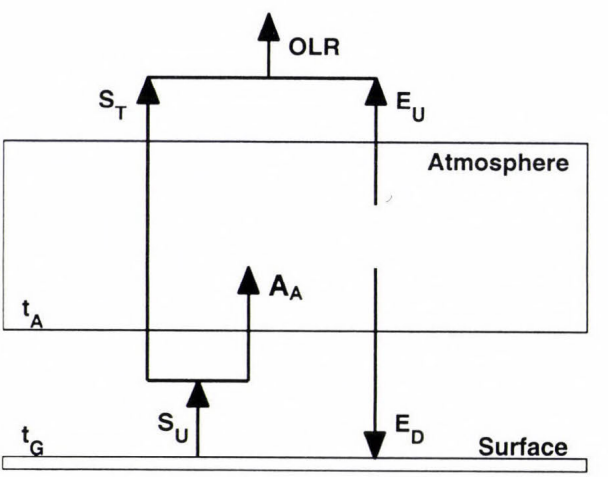

Fig. 2. IR rdiative transfer model of the atmosphere. The definitions of the flux density components are included in Table 1. t_A is the surface air temperature, t_G is the surface temperature. In the simulation t_A and t_G was set to be equal, $t_S = t_A = t_G$, where t_S is the thermal equilibrium temperature.

It has been recognized for a long time, that the far infrared part of the OLR plays an important role in the Earth radiation budget. However, due to the lack of the operational observation of the FIR spectral range, the global picture of the terrestrial radiation field is not yet complete. With our recent work we will try to fill up this gap with high accuracy LBL computations of the FIR, MIR, and WIN flux density components for a set of carefully selected atmospheric profiles from around the globe. In the next section the details of the input database and the parameters of the simulation are discussed.

Table 2. Comparisons of the FIR part of total greenhouse forcing (%)

Atmosphere	**This calculation**			***Brindley* and *Harries* (1997)**
	FIR: 1–560 cm^{-1}	**FIR: 1–660 cm^{-1}**	**FIR: 1–720 cm^{-1}**	
Tropical	36	43	54	25
Subarctic winter	43	53	68	33

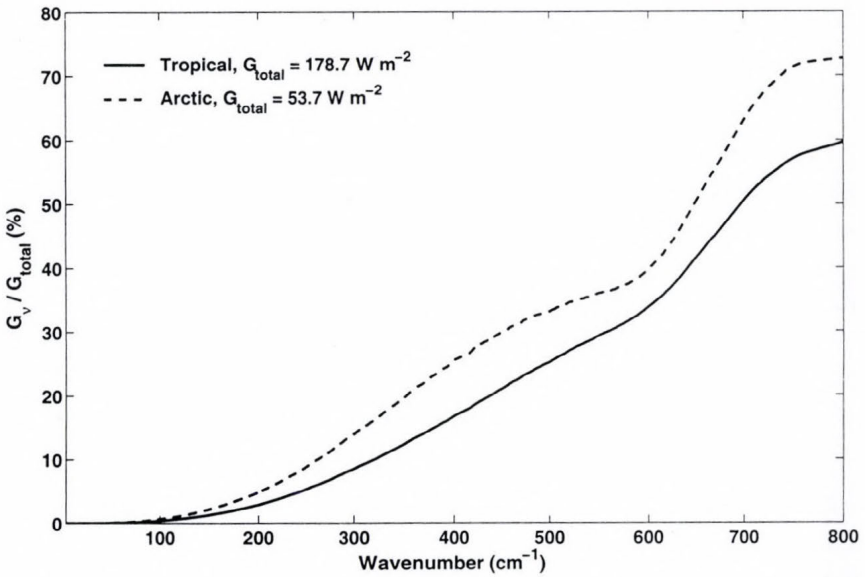

Fig. 3. The dependence of relative FIR spectral greenhouse factor on wave number. This figure demonstrates the importance of the definitions of the spectral boundaries.

2. *Global data set and LBL simulation*

Our qualitative estimates of the meridional distributions of the FIR, MIR, and WIN flux density components were based on a representative subset of the TIROS Initial Guess Retrieval (TIGR), global radiosonde archive (*Chedin* and *Scott*, 1983). From the TIGR archive, about 230 atmospheric profiles were extracted in a way that the temporal and spatial statistical characteristics of the original data set were preserved. The profiles were chosen regardless of the surface type. The surface emissivity was set to unity and the temperature of the emitting surface (t_G) was set to the temperature of the lowest atmospheric level (t_A): $t_S = t_A = t_G$, where t_S is the common temperature. The global average surface temperature and water vapor column amount (w) are 285.3 K and 2.53 precipitable cm (prcm), respectively. Further on we shall use the term "global avareage" to indicate that the average value is computed from zonal mean values weighted with the cosine of the latitude. It is usually hard to tell how representative a data set for global and annual climatology research is. We believe, that our data set contains sufficient information to characterize the contributions of different spectral ranges to the meridional distributions of the total and spectral clear-sky flux density components. Here we note, that the temperature profile set represents real equilibrium situations, where all kind of energy sources and sinks in the layered atmosphere are balanced by IR radiative cooling or heating. More details on the profile selection strategy can be found in *Miskolczi* and *Rizzi* (1998).

For the radiative transfer computations we used the High-resolution Atmospheric Radiative Transfer Code (HARTCODE), (*Miskolczi et al.*, 1990). More results on the validation of HARTCODE may be found in *Rizzi et al.* (2002) and *Kratz et al.* (2005). Here we shall not go into the full details of an LBL simulation, but summarize only a few important basic features. This work partly uses the results of a previous study performed to evaluate the temperature and water vapor sounding capabilities of the Advanced Earth Observing Satellite (ADEOS2) Global Imager (GLI) instrument, and therefore, particulars of the LBL simulations were already reported in *Miskolczi* and *Rizzi* (1998).

A large data set of directional radiances and transmittances computed for the TIGR profiles and GLI spectral range, (800–2800 cm^{-1}), with 1.0 cm^{-1} spectral resolution were already available. To obtain the total flux densities, additional radiance computations were done for the spectral ranges not covered by the GLI instrument. The directional radiances were determined in nine streams, and assuming cylindrical symmetry, a simple code was developed to facilitate the integration over the solid angle.

For the spectral range covered by the GLI instrument the GEISA (*Husson et al.*, 1994), absorption line compilation were used and for the remaining part of the spectra we used the HITRAN2K line catalog (*Rothman et al.*, 1998; *HITRAN2K*, 2002).

The atmosphere was stratified using 32 exponentially placed layers with about 100 m and 10 km layer thickness at the bottom and the top, respectively. The full altitude range was set to 61 km and the slant path was determined by spherical refractive geometry. The upward and downward slant path were identical, which assured that the directional spectral transmittances for the reverse trajectories were equal. Altogether eleven absorbing molecular species were involved: H_2O, CO_2, O_3, N_2O, CH_4, NO, SO_2, NO_2, CCl_4, F11, and F12.

The H_2O continuum absorption parameterization was similar to the CKD2.4 without the slight recent adjustments made in some part of the far infrared range (*Tobin et al.*, 1999). In the most affected spectral ranges of the CO_2 Q bands, the line-mixing effects were considered using a recent line-mixing parameterization by *Rodriguez et al.* (1999). No adjustments were implemented for the non-local thermodynamic effects and the effects of the aerosols were also ignored.

The direct output from HARTCODE were the spectral atmospheric upward emittance ($E_{\nu,U}$), downward emittance ($E_{\nu,D}$), surface upward flux density ($S_{\nu,U}$), and the atmospheric flux transmittance ($Tr_{\nu,A}$). The atmospheric spectral flux transmittance, by definition, is the ratio of the transmitted flux density ($S_{\nu,T}$) to the surface upward flux density: $Tr_{\nu,A} = 1 - A_\nu = S_{\nu,T} / S_{\nu,U}$, where A_ν is the spectral flux absorptance. The spectral outgoing longwave radiation is taken as the sum of the transmitted flux density and atmospheric upward emittance, $OLR_\nu = S_{\nu,T} + E_{\nu,U}$. The spectrally integrated and/or averaged quantities are indicated by omitting the subscript ν. The definitions of other derived quantities are given in *Fig. 2* and *Table 1*.

The ratio of the *OLR* to the surface upward flux density is sometimes called flux transmittance or total flux transmittance (Tr_T). To distinguish this quantity from the atmospheric flux transmittance, further on we shall call this quantity terrestrial flux transmittance: $Tr_T = OLR/S_U$. We use the term "total" to indicate integration over the 1–3000 cm^{-1} spectral range. In *Table 3* we present the basic statistics and global averages of the computed S_U, E_D, OLR, S_T, and G parameters.

Throughout this paper we frequently refer to figures with one or more parameterized functions. To make the reference to those parameterized functions easier, we supplied their serial number with a prefix character (#)

and included them into *Table 4*. When referencing to them only their special serial numbers are quoted.

Table 3. Basic statistics and global averages of the flux density components (W m^{-2})

Spectral regions	Parameters	S_U	E_D	*OLR*	S_T	*G*
Total	Minimum	165	103	150	22	5.9
	Maximum	521	429	297	112	223
	Mean	313	235	223	69	89
	Standard	82	82	34	13	49
	Global	382	309	250	61	132
FIR	Minimum	112	89	100	0.0	4.2
	Maximum	244	241	140	29	120
	Mean	173	166	119	7.0	54
	Standard	31	37	8.0	7.2	25
	Global	199	195	123	2.6	75
MIR	Minimum	7.4	6.6	6.0	0.7	0.4
	Maximum	79	73	21	2.8	63
	Mean	31	29	11	1.4	20
	Standard	16	16	3.0	0.3	14
	Global	45	43	14	1.3	31
WIN	Minimum	46	8.0	44	21	1.3
	Maximum	198	139	157	108	47
	Mean	109	40	93	61	16
	Standard	35	32	25	13	11
	Global	138	71	113	57	25

3. Results and discussion

3.1 Outgoing logwave radiation

One may not expect that a limited data set of 230 profiles will reproduce accurately the detailed meridional picture, especially around the highly variable ITC zone. However, it is possible to characterize the average behavior and tendency of the meridional variation by the zonal means or by a smooth curve - usually a low order polynomial or spline - fitted to the zonal means. This is clearly demonstrated in *Fig. 4,* where the simulated zonal mean *OLR* from the TIGR data set are compared to the mean clear-sky and all-sky meridional distributions obtained from the ERBE measurements.

Table 4. Parameterized functions in the Figures, (u=ln(w))

Fig.	X	Y	Curve	Function Y = f(X)	r	No.
7	u	Tr_A	Total	$\exp(-1.461 - 0.2819\,x - (1231\,x^2 + 541.9\,x^3 + 84.66\,x^4)/10^4)$	0.993	#1
			FIR	$\exp(-4.292 - 2.255\,x - 0.8324\,x^2 - 0.1781\,x^3 - 0.01521\,x^4)$	0.998	#2
			MIR	$\exp(-3.190 - 0.5659\,x + 0.02778\,x^2 + 0.01022\,x^3 - 0.0007153\,x^4)$	0.998	#3
			WIN	$\exp(-0.2249 - 0.2543\,x + 0.01545\,x^2 - 0.007840\,x^3 + 0.0007537\,x^4)$	0.994	#4
8	u	τ_A	Total	$\exp(0.3833 + 0.1908\,x + 0.05183\,x^2 + 0.01988\,x^3 + 0.002399\,x^4)$	0.992	#5
			FIR	$\exp(1.45 + 0.523\,x + (744\,x^2 - 43.1\,x^3 - 86.2\,x^4 - 19.14\,x^5 - 0.776\,x^6)/10^4)$	0.996	#6
			MIR	$\exp(1.161 + 0.1765\,x - 0.02598\,x^2 + 0.0004931\,x^3 + 0.0008610\,x^4)$	0.997	#7
	w		WIN	$0.2214 + 0.2611\,x$	0.992	#8
9	u	τ_T	Total	$\exp(-1.098 + 0.3055\,x)$	0.896	#9
			FIR	$\exp(-0.9682 + 0.3\,x)$	0.884	#10
			MIR	$\exp(-0.009824 + 0.2281\,x)$	0.834	#11
			WIN	$\exp(-1.912 + 0.3473\,x)$	0.903	#12
10	Tr_F	Tr_T		$0.09922 + 0.9043\,x$	0.997	#13
14	w	R_U	Total	$0.4961 + 0.0009681\,x$	0.028	#14
			FIR	$0.7026 - .04167\,x + 0.002596\,x^2$	0.658	#15
	u		MIR	$\exp(-1.1101 - 0.216\,x)$	0.738	#16
	w		WIN	$0.1311 + 0.1276\,x - 0.008184\,x^2$	0.975	#17
17	u	R_D	Total	$0.7371 + 0.06411\,x + 0.0156\,x^2 + 0.003123\,x^3$	0.947	#18
	w		FIR	$1 - 0.52071\exp(-3.213\,x^{0.4555})$	0.965	#19
			MIR	$1 - 0.6766\exp(-2.293\,x^{0.1656})$	0.842	#20
			WIN	$-1.518 + 1.67\exp(0.09220\,x - 0.006403\,x^2)$	0.987	#21
30	u	dt_G	Total	$22.32 + 7.921\,x + 0.86\,x^2$	0.913	#22
			FIR	$11.59 + 3.177\,x + 0.22\,x^2$	0.892	#23
			MIR	$1.163 + 0.4868\,x + 0.06251\,x^2$	0.931	#24
			WIN	$9.566 + 4.256\,x + 0.5768\,x^2$	0.917	#25
		dt_E	Total	$23.46 + 7.376\,x + 0.6058\,x^2$	0.886	#26
32	u	dt_A	Total	$17.43 - 4.552\,x - 1.178\,x^2 - 0.1971\,x^3 + 0.02624\,x^4$	0.982	#27
			FIR	$12.28 - 4.614\,x - 0.6769\,x^2 - 0.01734\,x^3 + 0.03412\,x^4$	0.994	#28
	w		MIR	$2.023 + 0.2647 - 0.1893\,x + 0.01746\,x^2$	0.727	#29
			WIN	$2.254 + 1.089 - 0.3753\,x + 0.02855\,x^2$	0.795	#30
	dt_A	t_S	Total	$302.7 - 0.08994\,x - 0.08778\,x^2$	0.869	#31

The correlation coefficient (r) is defined as: $r = (1 - \sigma^2_R / \sigma^2_Y)^{0.5}$, where σ_R is the residuum standard deviation.

The top and bottom curves in this plot were obtained by fitting a third order polynomial to the zonal averages of about 70,000 all-sky and 40,000 clear-sky annual average *OLR* measurements from the ERBS, NOAA9, and NOAA10 satellites. The markers in this figure are the TIGR OLR fluxes averaged over latitudinal belts of 5-degree widths.

The total *OLR* curve from the TIGR data set is between the clear-sky and all-sky *OLR* curves from the ERBE, and the shape of the curves are very similar.

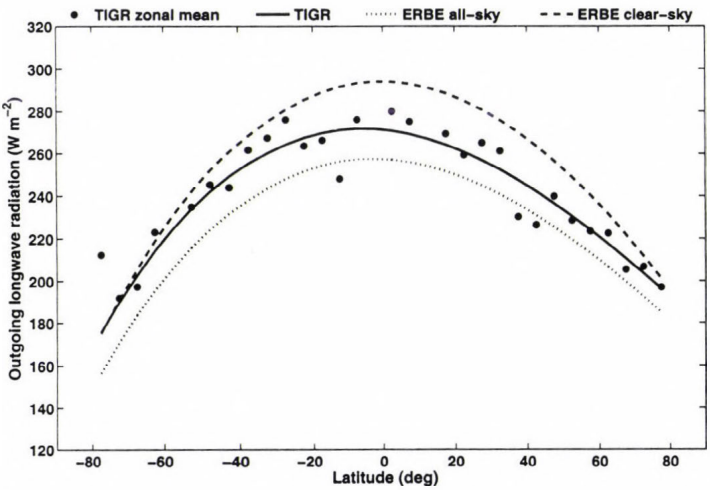

Fig. 4. Computed and measured *OLR*. The dotted and dashed curves are third order polynomials fitted to the ERBE clear-sky and ERBE all-sky zonal mean data points (ERBE, 2004).

Considering the surface temperature and emissivity settings in this simulation, this figure shows a remarkable agreement with the ERBE data set. The global averages of the *OLR*s are 250, 268, and 236 W m^{-2} for this simulation, the ERBE clear-sky and ERBE all-sky cases, respectively.

Fig. 5 shows the spectral decomposition of the *OLR*. The decreasing total *OLR* toward the poles are mainly due to the reduced upward fluxes in the WIN region. To a somewhat lesser extent, the FIR and MIR spectral regions also contribute to the poleward reduction of the total *OLR*. This is an indication of the presence of relatively small amounts of transmitted surface fluxes. Compared to the total *OLR*, the poleward variation in the FIR part is surprisingly small, not exceeding 5–7%.

The total *OLR* contains the FIR *OLR* and, therefore, theoretically there should be a strong correlation between the two quantities. According to our

data set, a linear relationship exists between the total and FIR *OLR* with a 0.88 correlation coefficient. Utilizing this relationship, we estimated the FIR component of the ERBE clear-sky *OLR*, and plotted it in *Fig. 5* as dots. In the plot, due to the large number of data points, the dots are organized into short vertical "bars". The vertical extensions of the bars indicate the variability of the ERBE FIR *OLR*s at a given latitude. The distances between the bars are 2.5 degrees, corresponding to the latitudinal resolution of the ERBE archive.

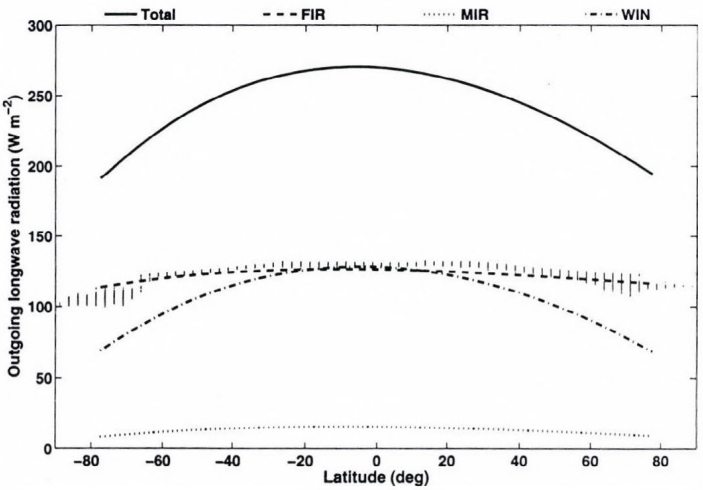

Fig. 5. Latitudinal distributions of the total and spectral components of the outgoing longwave radiation. The FIR and MIR components have very small latitudinal variation. The short vertical 'bars' are the estimated five year average ERBE FIR *OLR*.

Since it is known a-priori, that the surface and atmospheric temperatures are significantly decreasing poleward, the more or less constant meridional TIGR and ERBE FIR *OLR* must be the result of a delicate compensation mechanism. The interesting question is how the surface temperature, temperature and humidity profiles, and the atmospheric spectral transparency are linked together to produce the above phenomenon.

3.2 Flux transmittance and graybody optical thickness

The atmospheric transparency is increasing with decreasing absorber amount. In the Earth's atmosphere water vapor is the major absorber, therefore, the meridional distribution of Tr_A must obey the poleward decrease of the water vapor column amount. As it is evident from *Fig. 6*, the total, MIR, and WIN

components of Tr_A are increasing poleward, while the FIR part is effectively zero in the equatorial regions, reaching only 10% at the poles. The MIR Tr_A behaves similarly, except, it is always larger than zero because of the presence of larger transparent regions within the MIR spectral range.

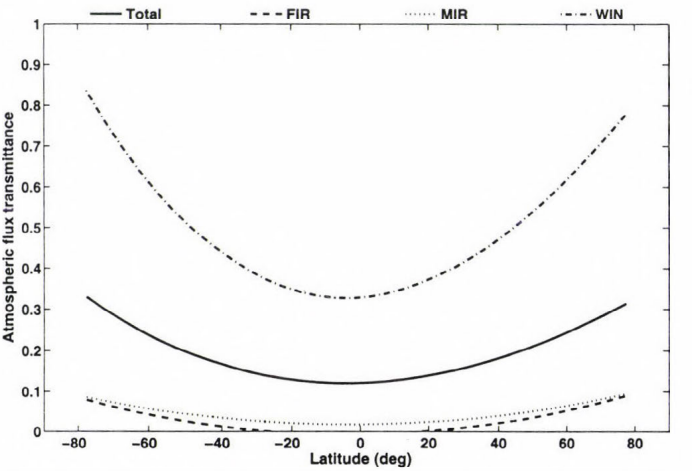

Fig. 6. Latitudinal distributions of the total and spectral components of the atmospheric flux transmittance, $Tr_A = S_T/S_U$.

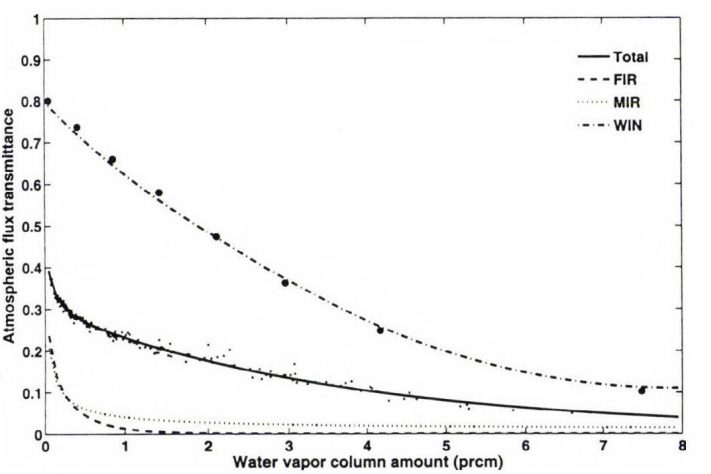

Fig. 7. Dependence of total and spectral atmospheric flux transmittance components on water vapor column amount. The large dots are the parameterized WIN Tr_A functions tested with an independent set of eight profiles.

In *Fig. 7* the total and spectral components of the Tr_A are plotted as the function of w. The small dots are for the total Tr_A. The parametrization of Tr_A with the water vapor column amount is of common interest. Eqs. #1 – #4 are the appropriate functions that reproduce Tr_A with a residuum correlation coefficient better than 0.995. The validity of Eq. #4 was tested with an independent profile set consisting of five climatological average profiles, the USST 76 atmosphere, and two extreme TIGR profiles. The computed window transmittances are marked by larger dots. Obviously, Eq. #4 is valid for the full range of w in the Earth's atmosphere.

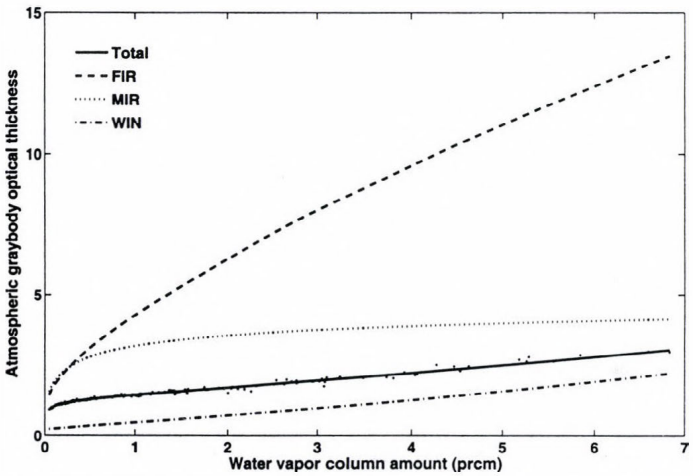

Fig. 8. Dependence of total and spectral atmospheric graybody optical thickness, $\tau_A = -\ln(S_T / S_U)$, on water vapor column amount.

By definition, the atmospheric graybody optical thickness (τ_A) is expressed as: $\tau_A = -\ln(Tr_A)$. The dependence of the total and spectral τ_A on w is displayed in *Fig. 8*, and the relevant parameterized formulas are given by Eqs. #5 – #8. For the total τ_A the original data points are also plotted. The important message of this figure is the fact, that due to the saturation tendency of the FIR and MIR Tr_A, above 1 prcm water vapor column amount (see also *Fig. 7*), the total atmospheric optical thickness is increasing according to the increase in the WIN component. We have a pretty good linear relationship for the WIN τ_A and, in the 0.5–7 prcm range of w, the linear relationship for the total τ_A is also a good approximation.

Using the terrestrial flux transmittance, it is also possible to define an effective terrestrial graybody optical thickness (τ_T): $\tau_T = -\ln(Tr_T)$. The

dependence of τ_T on w is shown in *Fig. 9*. The parameterized functions are Eqs. #9 - #12. The scattered dots belong to the total τ_T. Apparently, the scatter of the data is larger than in the case of τ_A, and there is a very limited range of w where a linear relationship would hold. The practical importance of this parameter is related to the fact that the *OLR* and S_U are readily available from satellite observations, therefore, Tr_T and τ_T can easily be derived on a global scale.

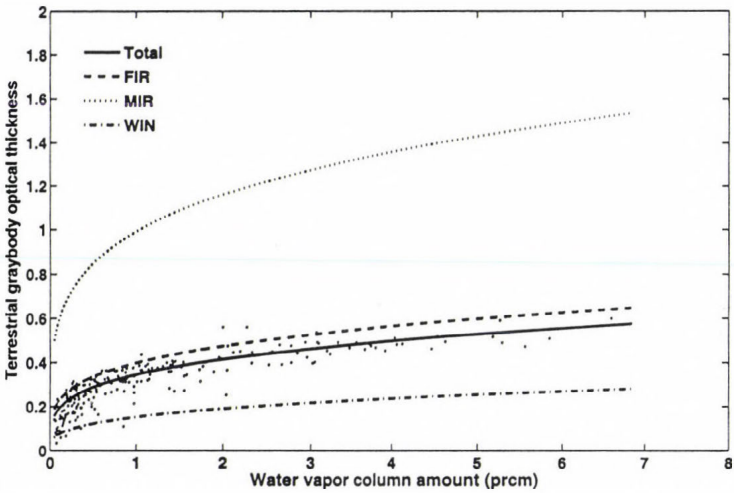

Fig. 9. Dependence of total and spectral terrestrial graybody optical thickness, $\tau_T = -\ln(OLR / S_U)$, on water vapor column amount.

The spectral components of Tr_T were also studied. The total Tr_T and its spectral components are presented in *Fig. 10*. The strong correlation of the total with the FIR Tr_T could be very useful for practical purposes. Probably this relationship could be improved by adjusting the FIR spectral limits. Based on this strong linear dependence, it is possible to derive the total *OLR* from observations of the FIR *OLR* alone and, perhaps, the surface temperature. This relationship could also work in the opposite direction, and the FIR flux density may be derived from the total *OLR*. Although Tr_T has not much physical meaning (as transmittance), later we shall see that Tr_T is closely related to the IR atmospheric transfer function. Generally speaking, the atmosphere modulates the surface upward flux density by absorption and emission. In radiative equilibrium, theoretically, the transfer function fully accounts for the combined absorption/emission effects and, therefore, Tr_T could be used for the large scale global estimate of the graybody optical thickness.

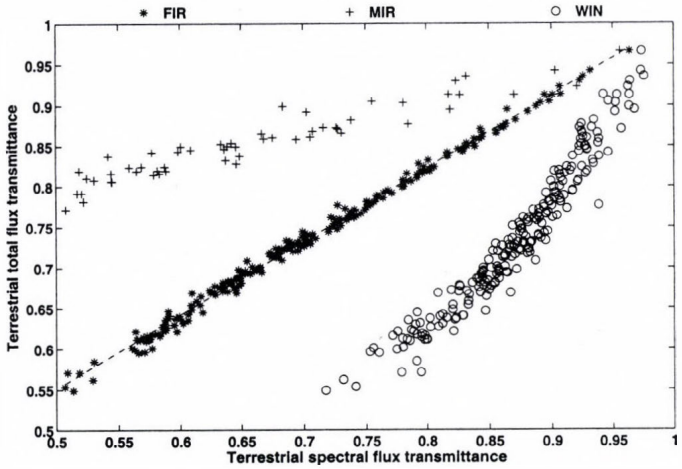

Fig. 10. Terrestrial total flux transmittance and its spectral components. The relatively larger scatter of the MIR and WIN data points are indication of increased S_T in those spectral ranges.

3.3 Transmitted surface radiation and atmospheric emittance

While the *OLR* can easily be measured with sufficient accuracy by satellite radiometers, the transmitted flux density and the upward atmospheric emittance can only be derived by lengthy computations of the accurate spectral flux transmittance.

The transmitted spectral flux density from the surface and the atmospheric upward emissivity may be written as $S_T = S_U Tr_A$ and $E_U = OLR - S_T$, respectively. The meridional distribution of the total S_T and its spectral components are presented in *Fig. 11*. It is not a surprise that the total S_T is governed by the WIN component, however, the latitudinal distribution of the WIN and the total S_T is very interesting. From the equatorial regions to about +/- 60° latitudes, S_T is increasing despite the large poleward decrease in the surface temperature. Proceeding toward the arctic regions, S_T will drop again considerably. The explanation for this unique behavior lies in the relative rate of the poleward decrease of the surface temperature and poleward increase of atmospheric transparency. After about +/- 60° latitudes, the temperature decrease will be the dominant factor.

This latitudinal dependence of S_T has an implication on its temperature dependence. Namely, the transmitted surface radiation is not increasing monotonously with the surface temperature, but must have a maximum value at around 270 K, representing the +/- 60° latitudes, see *Fig. 12*. Further on, this also implies that from +/- 60° latitudes toward the equator the surface net

radiation (atmospheric downward minus surface upward) will increase with increasing t_S. The above phenomenon is called "super-greenhouse effect" (*Vonder Haar*, 1986), and it is controlled by the strong H_2O continuum absorption in the windows region and the meridional distributions of w. At the polar regions or beyond +/– 60° latitudes, the longwave total net surface flux density is decreasing with increasing t_S, meaning, that the rate of warming of the surface by the downward atmospheric emittance is less efficient than the rate of energy loss of the surface.

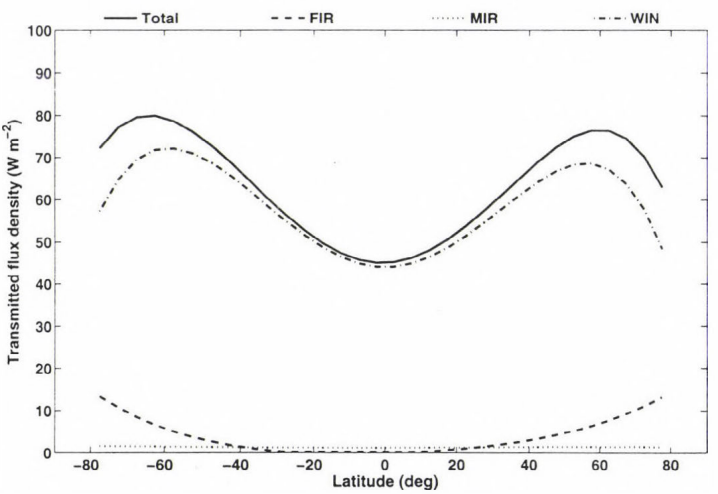

Fig. 11. Latitudinal distributions of the total and spectral components of the transmitted flux densities.

In *Fig. 11* the FIR component has a steady rise toward the poles from about +/– 20–30° latitudes. The little asymmetry in the region of the total absorption around the equator is related to the asymmetry in the latitudinal distribution of w. The contribution to the total S_T from the MIR spectral range is not significant (1–2 W m^{-2}) and does not change much along the latitudes.

The latitudinal variation of the FIR and WIN E_U are displayed together with the FIR and WIN *OLR* in *Fig. 13*. The FIR *OLR* is largely made up by the FIR E_U. In the polar regions the transmitted surface flux contributions may reach 15–20%. The WIN E_U contributions to the WIN *OLR* is decreasing poleward, up to +/– 65° latitudes. At higher latitudes there is a small increase in the WIN E_U, which could be the consequence of relatively higher temperatures in the lower troposphere due to frequent temperature profile inversions.

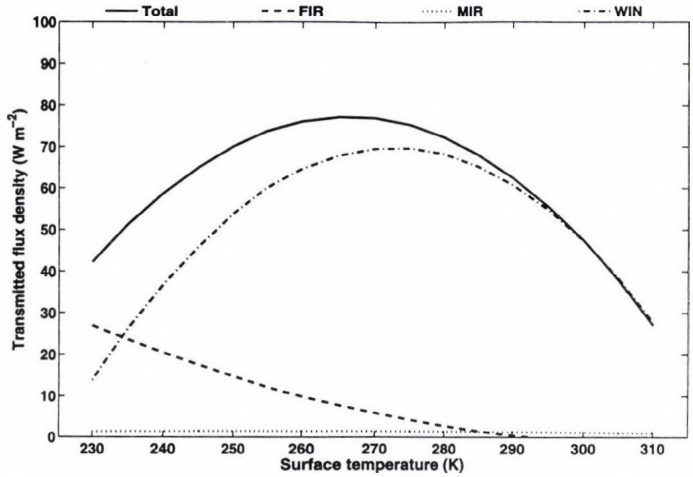

Fig. 12. Dependence of transmitted flux density on surface temperature. As a consequence of the peaks in the transmitted flux densities around +/–60° latitudes in Fig. 11, the total and WIN Tr_A functions have maximums at around t_S = 270 K.

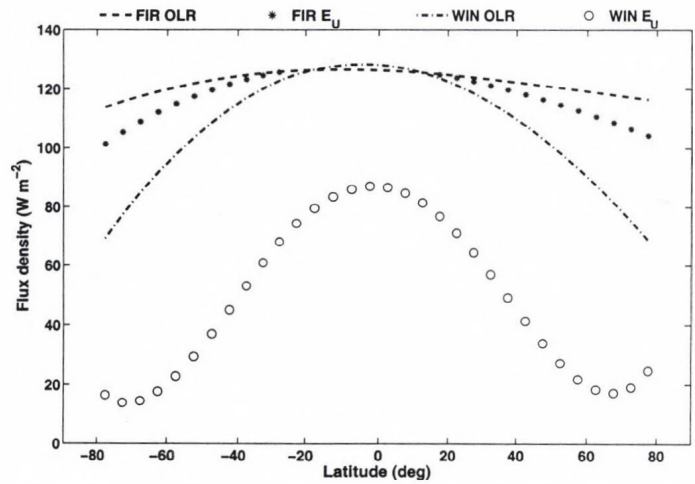

Fig. 13. Latitudinal distributions of the total, FIR, and WIN *OLR*s and the FIR and WIN upward atmospheric emittance.

The normalized atmospheric upward emittance (R_U) is an excellent parameter for studying the role of the atmospheric absorption in the different spectral regions: $R_U = E_U / S_U = Tr_T - Tr_A$. In *Fig. 14* the total and spectral

components of R_U are displayed as the function of w. The dots in this figure indicate the original FIR data points. The smooth curves are the plots of Eqs. #14 - #17. As is evident, the total zonal mean R_U is almost independent of w, see the low regression coefficient of Eq. #14. This figure actually suggests that, the zonal averages of the total upward atmospheric emittances are practically independent of w, and they may be taken as half of the surface upward flux densities. This is a clear indication that for zonal means, the assumption of radiadiative equilibrium approximately holds. Computed from the local S_U and E_U data, the global average E_U/S_U ratio is 0.495. Using the emissivity approximation, it can easily be shown, that the trivial solution for homogeneous atmosphere is 0.5 (see for example *Goody* and *Yung*, 1989). It can also be shown that in case the surface temperature and surface air temperature is equal, the theoretical ratio (R'_U) depends only on the graybody optical thickness: $R'_U = \hat{f} - Tr_A = A - \hat{g}$, where A is the flux absorptance and by definition, $\hat{f} = 2/(1 + \tau_A + Tr_A)$ is the atmospheric transfer function and $\hat{g} = 1 - \hat{f}$ is the greenhouse function. In *Fig. 15* the theoretical and some simulated ratios are compared. The global average of the R'_U factor is 0.496, which is in excellent agreement with the average R_U. The good agreement in the global averages is not a surprise, because of the planetary radiative equilibrium requirement. However, the existence of the radiative equilibrium for the zonal means is more interesting.

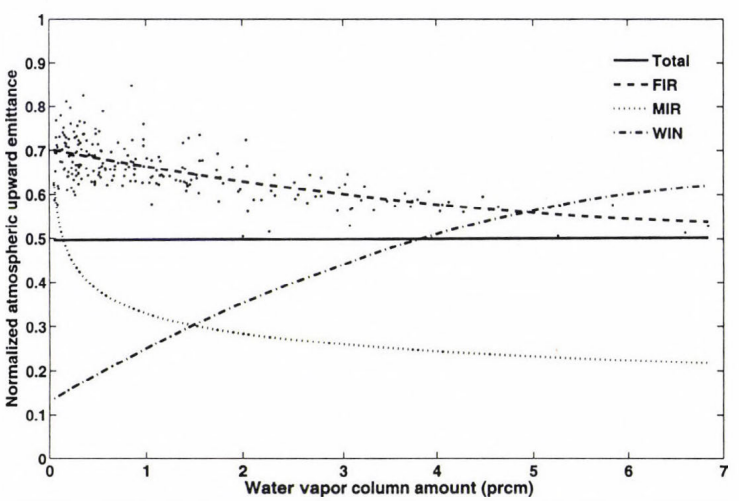

Fig. 14. Dependence of normalized atmospheric upward emittance on water vapor column amount.

In *Fig. 14* the FIR, MIR, and WIN part of R_U are varying significantly with w. The FIR and MIR components are decreasing with increasing w, while the WIN component shows the opposite effect. The physical explanation of these facts are very simple. In case of the opaque spectral regions like FIR and MIR, increasing w results in decreasing atmospheric transparency. This must be coupled with the upward shift of the weighting functions, and therefore, assuming a negative vertical temperature gradient, the effective atmospheric emittance will be shifted to colder atmospheric layers. This process will also explain the unusually small meridional variation in the FIR and MIR *OLR*s.

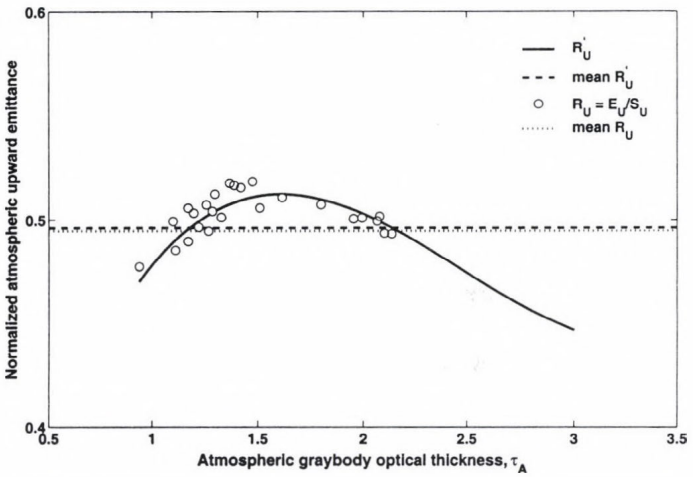

Fig. 15. Theoretical and simulated normalized upward emittance. The horizontal lines are global averages.

To make this point more clear and to quantify the process, test calculations were performed for the tropical and subarctic winter atmospheres. We have computed the weighting functions in the strongly absorbing part of the FIR region with the spectral resolution of 0.25 cm^{-1}. In plot A of *Fig. 16* the differences in the altitudes of the peak values (arctic-tropical) are shown as the function of the wave number. On average, there is about 2.5 km down-shift in the FIR spectral region. At some narrow spectral interval, the opposite effect may also be observed. In plot B the spectrally averaged weighting functions are presented, again showing the down-shift. The slightly different H_2O continuum coefficients in the FIR region, (CKD 0 and CKD 2.4) have no effect on the conclusions of the qualitative picture. The average peak positions were moving from about 7.7 km, in the case of the tropical atmosphere to about 5.2 km in the case of the arctic winter atmosphere. Apparently, the peaks are always above a possible low level inversion and below the stratospheric temperature

rise, even if we consider the lowering of the height of the tropopause toward the poles. The thermal structure of the atmosphere between the 5 and 10 km altitude range or up to the tropopause is usually characterized with a negative temperature gradient explaining the increasing FIR and MIR R_U with decreasing w (in *Fig. 14*). As an indirect evidence of the above process, by the simulation of the response of the *OLR* of the arctic winter atmosphere to the decrease in the H_2O continuum absorption coefficient in the FIR spectral range, it was shown in *Tobin et al.* (1999) that the top of the atmosphere flux density increases.

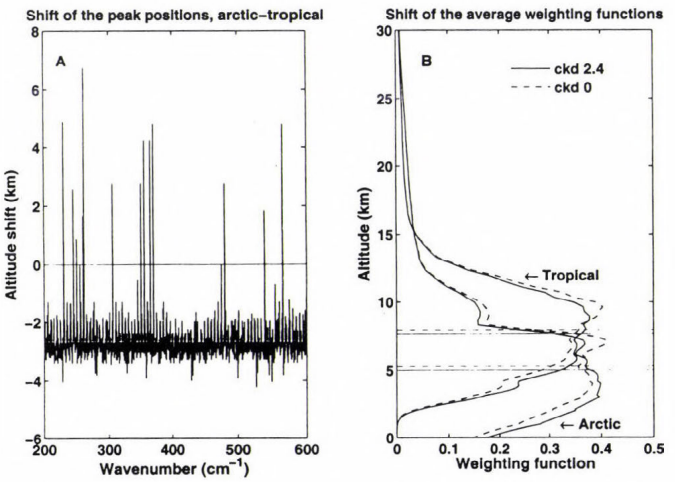

Fig. 16. Relative position of the peak of the FIR spectral weighting functions (plot A) and the average FIR weighting functions (plot B). Note the relatively small effect of the changes in the H_2O continuum parameterization in plot B.

The explanation of the behavior of the WIN R_U is also simple. Since the whole vertical atmosphere contributes to the E_U, its increasing value with increasing w indicates, that larger w is usually associated with warmer atmosphere, and the fractional amount of the upward re-emitted radiation is roughly proportional to the absorbed radiation. The WIN Tr_T does not change very much; the global average is 0.8544 and the standard deviation is about 6%. Consequently, the relationship $R_U \sim 0.8544 - Tr_A$ means, that the relative upward atmospheric windows emittance depends only on the total absorption.

Just for completeness, in *Fig. 17* the total and spectral normalized atmospheric downward emittances (R_D) are presented as the function of w, see also Eqs. #18 – #21. R_D is computed similarly to R_U, but using the atmospheric downward emittance : $R_D = E_D / S_U$. According to the Kirchoff's law, R_D may be identified as the clear-sky total graybody absorptance: $R_D = 1 - Tr_A = A$. For

the recent TIGR profile set - which contains some very cold and dry as well as very warm and humid profiles - R_D varies between 0.63 and 0.93. The only interesting feature of this figure is the saturation of the FIR R_D at around 2 prcm water vapor column amount. The sharp decrease in R_D with decreasing water vapor content is the result of the opening up of the so called "micro windows" in the FIR spectral region as it was also evidenced by the Surface Heat Budget of the Arctic Ocean, SHEBA, experiment (*Tobin et al.*, 1999). The FIR and MIR R_D may exceed one, which is the indication of cases with strong close to surface temperature profile inversions. The total R_D may be parameterized with quite a high accuracy using a third order polynomial of u, Eq. #18: $R'_D = f(u)$, where $u = \ln(w)$.

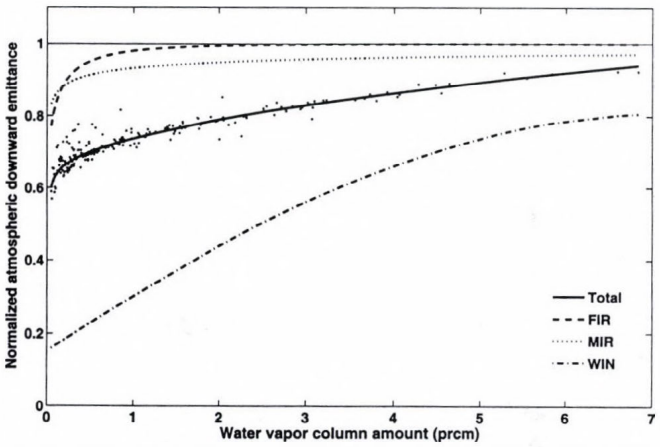

Fig. 17. Dependence of normalized atmospheric downward emittance on water vapor column amount.

E_D is an important term in the equation of the surface energy balance, and lots of efforts were devoted for its parameterization (*Brutsaert*, 1975; *Idso*, 1981; *Tuzet*, 1990). Using satellite observations of the air temperature at the surface and the water vapor column amount, together with the parameterized value of the clear-sky R_D by Eq. #18, the estimated downward emittance (E'_D) can easily be derived: $E'_D = \sigma t_A^4 R'_D$. The correlation coefficient between the true E_D and the parameterized E'_D is 0.998. There is some positive bias of 0.1%, and the 1 σ residuum standard deviation is 2.7%. While most of the commonly used empirical formulas fail at low temperatures and low water vapor content, and in the rare cases of very warm and dry profiles, the above parameterization gives pretty good fluxes even at extreme temperatures and water contents, see *Fig. 18* A and B.

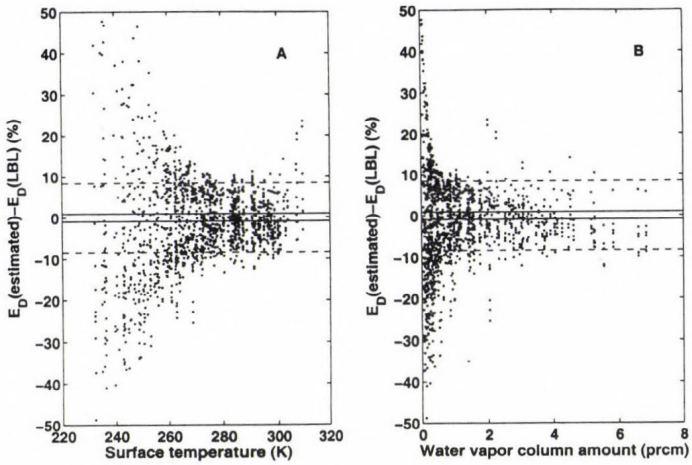

Fig. 18. Accuracy of the estimated downward atmospheric emittance calculated by bulk formulas and LBL simulations. Plot A shows the dependence on the surface temperature and plot B shows the dependence on the water vapor column amount. In both plots the dots represent the values computed by formulas of *Brutsaert* (1975) and *Idso* (1981). The dashed and solid lines are the standard deviations corresponding to the bulk formulas and LBL simulations, respectively.

In plot A of *Fig. 19* we have compared our parameterization with the highly sophisticated model of Gupta (*Gupta et al.*, 1992; *Gupta*, 1989). As it can be seen, the two parameterization compares very well. For further improvements we have developed a linear correction term to handle the temperature dependence. In case the information on the temperature and humidity profiles are available, one may calculate the effective temperature of the water vapor (t_H). Using t_A and t_H, our corrected formula may be written as: $E_D'' = E_D' - 32 + 0.857 t_A + t_H$. In plot B of *Fig. 19* E_D' and E_D'' are compared. The residuum correlation coefficient between E_D and E_D'' goes beyond 0.999, and probably sets the limit for the accuracy of simple parameterizations. The correction term seems to take care of almost all cases where the source of the differences were due to the low level temperature profile inversions. Further improvements seem to be difficult without building in more detailed temperature, water vapor, and ozone profile related information and breaking up the task for several shorter spectral intervals.

Such an increase of complexity is out of the scope of the recent paper. We have devoted much attention to the E_D parameter, but we shall see later, that through the $\tau_A \approx -\ln(1 - E_D / S_U)$ relationship we have the key for the large scale surface observation of the greenhouse effect or the IR equilibrium state of the atmosphere. For example, based on the CERES Ocean Validation

Experiment, (COVE), year 2002 time synchronized one minute archive of the E_D and S_U fluxes (*COVE*, 2003) we have estimated the local annual average all-sky atmospheric graybody optical thickness. For the April, 2002–March, 2003 time period, the annual average all-sky τ_A is 2.06 with a 1 σ standard deviation of 40%.

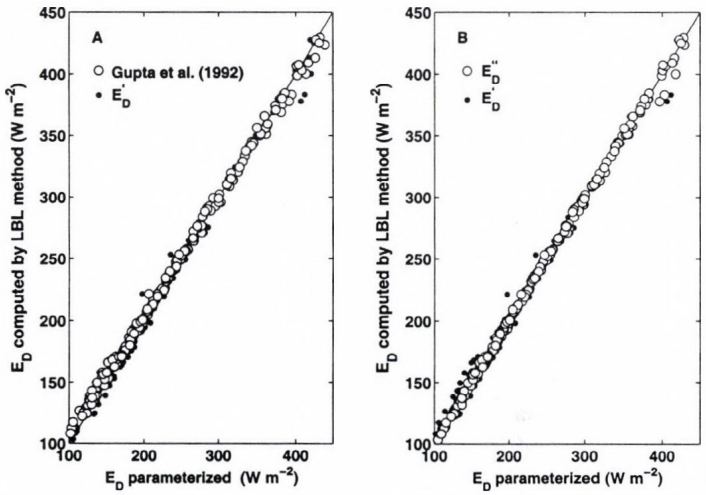

Fig. 19. Plot A is a comparison of E_D parametrizations by *Gupta* (1992) and the $E'_D = \sigma t_A^4 R'_D$ formula, where R'_D is a third order polynomial of $\ln(w)$, see Eq. #18 in Table 4. Plot B shows the effect of the temperature correction: $E''_D = E'_D + t_H - 0.857 * t_S - 32$, where t_H is the effective water vapor temperature.

Finally, in *Fig. 20* we summarize the two most important characteristics of the upward and downward emittances in the Earth's atmosphere:

- In the average sense the atmosphere is very close to the radiative equilibrium, and, as a consequence, the zonal and global average upward emittance is about half of the average surface upward flux density. This fact is supported by the recent assessment of the Earth's annual global mean energy budget by *Kiehl* and *Trenberth* (1997). Their estimates of S_U and E_U are 390 and 195 W m^{-2}, respectively.

- As a consequence of the Kirchoff's law, within the clear atmosphere the downward emittance is approximately equal to the absorbed flux density. Based on our data set, the global average clear-sky downward atmospheric emittance is 311.4 W m^{-2}, while the global average of the absorbed radiation by the clear-sky is 311.9 W m^{-2}. This equivalence – for

the highly variable atmospheric emission spectra and for global scale – was not shown before with such a high numerical accuracy. Utilizing the above two facts one may estimate the global (or zonal) average *OLR* with the simple expression: $OLR = 3E_U - E_D$.

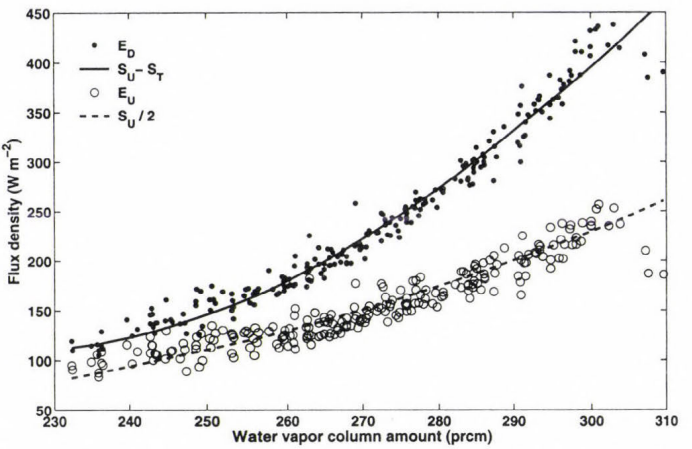

Fig. 20. Dependence of E_D and E_U fluxes on surface temperature. The solid line is a parabolic fit to the absorbed fluxes and the dashed line is the fit to the half of the surface upward fluxes.

4. Greenhouse effect

4.1 Overview

Regarding the planetary greenhouse effect we must relate the amount of the atmospheric absorbers to the surface temperature. Assuming monochromatic radiative equilibrium, isotropy in both hemispheres and a semi-infinite plane-parallel gray atmosphere, the predicted air temperature at the surface (t'_A) and the surface temperature (t'_G) are given by the next two equations (*Goody* and *Yung*, 1989; *Paltridge* and *Platt*, 1976):

$$t'_A = \left[\frac{OLR}{2\sigma}(1+\tau_A)\right]^{\frac{1}{4}}, \tag{1}$$

and

$$t'_G = \left[\frac{OLR}{2\sigma}(2+\tau_A)\right]^{\frac{1}{4}}. \tag{2}$$

In the above equations τ_A is the total graybody atmospheric optical thickness, as usually defined in two stream approximations, $\tau_A = (3/2)\tau$, where τ is measured vertically. The atmospheric skin temperature (t_0') and the characteristic graybody optical thickness which defines the IR optical surface of the planet (τ_C') are:

$$t_0' = \left[\frac{OLR}{2\sigma}\right]^{\frac{1}{4}}, \tag{3}$$

$$\tau_C' = 1. \tag{4}$$

Eqs. (1)–(4) are usually referred as the solutions of the Schwarzschild-Milne equations, see more details in *Rozanov* (2001), *Rutten* (2000), or in *Collins II* (2003). We should note, that the terrestrial graybody optical thickness is not an accurate measure of the atmospheric absorption and can not be used in Eqs. (1) and (2). These equations are frequently quoted in the meteorological literature and even in textbooks, however, it is a mistake to use them to study the radiative equilibrium and greenhouse effect in the Earth's atmosphere.

For the real atmosphere, the semi-infinite solutions must be replaced with the solutions valid for the bounded atmosphere. With relatively simple computation (we do not present it here) it can be shown, that for a given *OLR* or E_U the surface air temperature and surface temperature are mutually dependent on each other: $OLR = \hat{f}(S_A A + S_G Tr_A)$ or $E_U = \hat{f} S_A A - \hat{g} S_G Tr_A$, where S_G and S_A are the surface upward flux densities at t_G and t_A temperatures, respectively. The *IR atmospheric transfer* and the *greenhouse* functions ($\hat{f}$ and $\hat{g}$) play fundamental role in the planetary greenhouse effect.

In our simulation, for having no surface temperature data, and making the definition of the greenhouse effect simpler, we set the equilibrium surface temperatures to the surface air temperatures, $t_G = t_A = t_S$. Note, that in the boundary layer the principle of energy minimum (or maximum entropy) works toward the thermal equilibrium. In this case the theoretical dependence of t_S on the transfer function $\hat{f}$ is:

$$t_S'' = \left[\frac{OLR}{\sigma \hat{f}}\right]^{\frac{1}{4}} = \left[\frac{OLR(1+\tau_A + e^{-\tau_A})}{2\sigma}\right]^{\frac{1}{4}} \tag{5}$$

In case the lower boundary condition is explicitly set by t_G, the atmospheric skin temperature will also depend on the surface temperature and total optical thickness:

$$t_0'' = \left[\frac{OLR\,(1+e^{-\tau_A}(1+\tau_A)) - 2e^{-\tau_A}\sigma t_G^4}{2\sigma(1-e^{-\tau_A})} \right]^{\frac{1}{4}}. \tag{6}$$

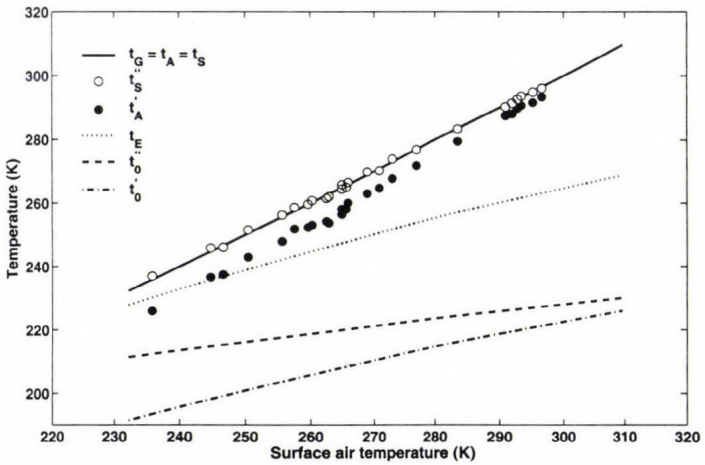

Fig. 21. Surface air, skin, and effective temperatures predicted by Eqs. (1), (3), (5), and (6). The dotted line is the effective temperature, $t_E = (OLR/\sigma)^{0.25}$. The symbols represent selected profiles with *OLR*s closest to the theoretical values.

In *Figs. 21* and *22* we compare the surface air and surface temperatures obtained by the different formulas. For reference, in *Fig. 21* the effective temperatures, $t_E = (OLR/\sigma)^{0.25}$, and the atmospheric skin temperatures are also plotted. Apparently, t_A' underestimates and t_G' badly overestimates the corresponding equilibrium surface and surface air temperatures. The error in t_A' decreases with increasing temperatures because of the increasing w (at higher temperatures). The atmospheric skin temperatures are also underestimated, and for the same reason the errors decrease with increasing temperatures.

The data points in these figures represent only about 10% of the total 230 profiles. Only those cases were selected for these plots, where the simulated and theoretically predicted *OLR*s agreed within less than 0.5%. Note, that (according to *Fig. 14*), for the zonal and global averages the radiative

equilibrium condition holds, but the individual profiles could be quite far from the radiative equilibrium. For example, it is obvious that profiles with temperature inversions will not fit into the theoretical picture which expects increasing temperatures with increasing optical thickness.

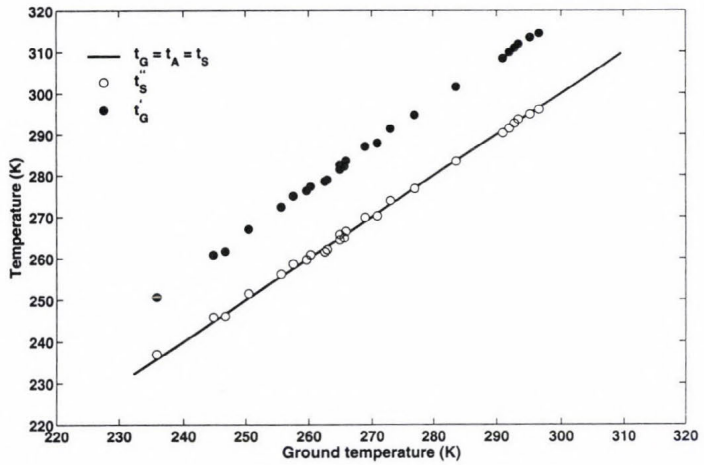

Fig. 22. Surface temperatures predicted by Eqs. (2) and (5). The symbols represent selected profiles with *OLR*s closest to the theoretical values.

In the bounded atmosphere the characteristic graybody optical thickness (τ_C'') becomes also dependent on the total optical thickness and surface temperature:

$$\tau_C'' = 1 - \frac{\tau_A - 2\left[\dfrac{\sigma t_G^4}{OLR} - 1\right]}{e^{\tau_A} - 1}. \tag{7}$$

In *Fig. 23* the τ_C'' and the simulated and theoretical atmospheric clear-sky graybody optical thicknesses are shown as the function of the surface temperature. The theoretical values (τ_A'') are the solutions of the transcendent equation for τ_A on the left hand side of Eq. (5). The τ_A'' and τ_A curves show excess optical thickness (water vapor) at very cold (arctic) and very warm (tropical) areas, while, there are optical thickness deficits at medium surface temperatures. With increasing temperature - or w -, τ_C'' tends toward the semi-infinite solution of 1.0. Sometimes τ_C'' is associated with an atmospheric altitude or pressure level of effective emission, see for example *Schneider et*

al. (1999). Since part of the *OLR* is, in fact, transmitted flux density from the surface, the physical meaning of such an atmospheric level is confusing. According to *Schneider et al.* (1999), the effective pressure level is between 540 and 600 hPa. Our computation shows a global average effective pressure level of 507 hPa. The global average effective pressure levels for the upward and downward atmospheric emissions are 339 and 666 hPa, subsequently.

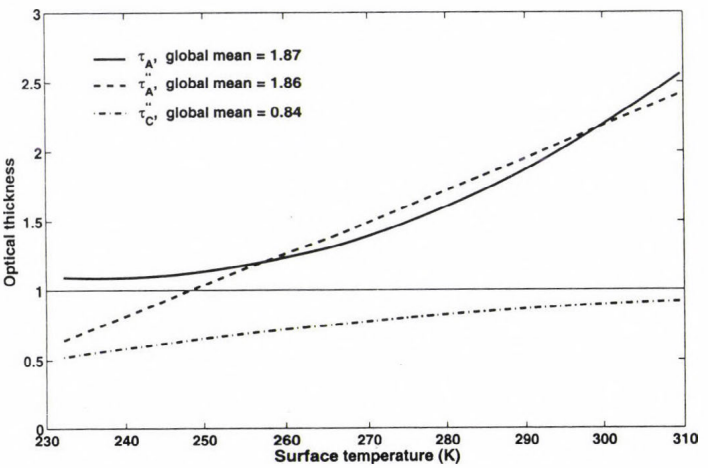

Fig. 23. Dependence of simulated and theoretical graybody optical thickness on surface temperature. The dash-dot line is the theoretical characteristic optical thickness, τ''_C, computed by Eq. (7).

The theoretical and simulated global average graybody optical thicknesses are in pretty good agreement: they are 1.87 and 1.86, and they correspond to a vertical optical thickness of about $\tau = 1.23$. These values are also the indication that the clear atmosphere loses its thermal energy close to the peak efficiency, see *Fig. 15*. Using Eq. (1) with the same data would result in about 9% higher optical thickness, and using Eq. (2) would result in an unrealistic low value of 0.67. Just for reference, if we use a global average surface and surface air temperature of 288 K and the ERBE global average clear-sky *OLR* of 268.0 W m^{-2}, the theoretically estimated vertical optical thickness would be 1.17, which is reasonably close to our global clear-sky average.

The atmospheric greenhouse effect is bounded to the absorption and emission of the IR radiation and controlled by the IR atmospheric graybody optical thickness. The keys to this parameter are the accurate (measured or modeled) atmospheric upward and downward flux densities, the correct computation of the atmospheric flux transmittances, and an adequate radiative

transfer model which relates the fluxes and flux transmittances. In the next section we shall shortly review the most commonly used greenhouse parameters and their relation to the atmospheric graybody optical thickness.

4.2 Greenhouse factor and normalized greenhouse factor

The most common measure of the greenhouse effect, which is also adopted by the global warming community, is the difference between the S_U and the *OLR*: $G = S_U - OLR$ (*Raval* and *Ramanathan*, 1989). The classical approach to the greenhouse effect is via the long-term energy balance equation of the solar radiation input and the IR radiation loss of the Earth surface. The difference between the effective planetary temperature – computed from the *OLR* or the solar input – and the global average surface temperature is the measure of the planetary greenhouse effect. In fact, the G factor is the application of the classical approach for the local flux densities without converting them to temperature differences. As we have seen in *Fig. 20*, the atmospheric absorption and the downward atmospheric emittance are approximately equal, therefore, the G factor can easily be related to the atmospheric upward and downward emittances: $G = S_U(1 - Tr_A) - E_U = E_D - E_U$. In case the surface air temperature and the surface temperature are equal, theoretically, the G factor is proportional to the product of S_U and the greenhouse function, which is only dependent on τ_A: $G = G(S_U, \tau_A) = S_U\, \hat{g}(\tau_A)$. The $\hat{g}(\tau_A)$ function may be expressed as:

$$\hat{g}(\tau_A) = \frac{\tau_A - 1 + e^{-\tau_A}}{\tau_A + 1 + e^{-\tau_A}}. \tag{8}$$

Eq. (8) shows the real physical meaning of the $g = G/S_U$ factor in *Raval* and *Ramanathan* (1989). The normalized greenhouse factor and the total atmospheric graybody optical thickness are uniquely related by the theory. For fixed absorber amounts the temperature sensitivity of $\hat{g}(\tau_A)$ – via the temperature dependence of the absorption coefficient – is very small due to the compensation effect through the τ_A and $\exp(-\tau_A)$ terms. In case of the standard tropical and arctic winter profiles, these sensitivities are –0.005 and –0.01% of $\hat{g}(\tau_A)$ per 1 K increase in the profile temperature. Obviously, these changes are negligible compared with the thermodynamic temperature dependence of the water vapor column amount on the temperature profile via the Clausius-Clapeyron equation, which has nothing to do with the temperature dependence of the greenhouse effect.

In *Fig. 24* we present comparisons of greenhouse factors obtained from the TIGR profile set and the ERBE data. The three versions of the G factor, $S_U - OLR$, $E_D - E_U$, and $S_U\,\hat{g}(\tau_A)$ are plotted as the function of surface temperature t_S. The ERBE annual averages were taken from *Raval* and *Ramanathan*, (1989) and they are plotted as open circles. Although we have some deviations at very large and small temperatures, this figure is actually an experimental proof of the validity of the theoretical $\hat{g}(\tau_A)$ function. The dependence of G on S_U also explains the high correlation with the surface temperature which was reported in *Raval* and *Ramanathan* (1989). For the sake of numerical comparisons, within the range of the ERBE data points, we calculated the regression lines of the $G_N(t_S)$, $u(t_S)$, and $G_N(u)$ linear functions. In *Table 5* the regression parameters are compared with similar ones in *Raval* and *Ramanathan* (1989). *Fig. 24* and *Table 5* show a very good overall agreement.

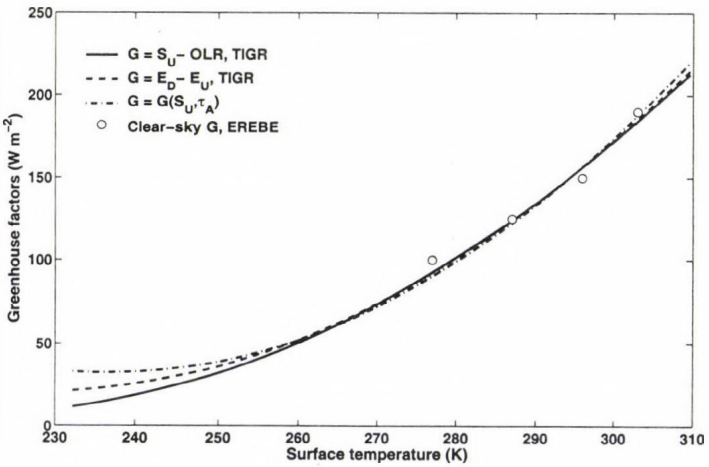

Fig. 24. Dependence of various greenhouse factors on surface temperature.

Table 5. Comparisons with *Raval* and *Ramanathan* (1989)

Parameter and equation	*Raval* and *Ramanathan*		This simulation		Correlation
	a	*b*	*a*	*b*	
$G_N = a * t_S + b$	0.00342	0.658	0.00465	-1.00	0.955
$u = a * t_S + b$	0.0553	-13.0	0.0588	-13.96	0.937
$G_N = a * u + b$	0.0576	0.155	0.0693	0.127	0.894

According to Eq. (8), the normalized greenhouse factor depends only on the total graybody atmospheric optical thickness. In *Fig. 25* we compare the $\hat{g}(\tau_A)$ function (solid line) with the G_N values (dots) obtained from our simulation. To show the general tendency of the simulated G_N, a smooth curve was fitted (dashed line) to the dots. Those cases which we marked as the closest ones to the state of radiative equilibrium are indicated with open circles. The global average $\hat{g}(\tau_A)$ and G_N are practically equal, $\overline{\hat{g}}(\tau_A) = \overline{G}_N = 0.33$, as it is expected from *Fig. 23*. We have seen already in *Fig. 8*, that the atmospheric graybody optical thickness grows almost linearly with the water vapor column amount. We have also shown a strong linear relationship between G_N and t_S in *Table 5*.

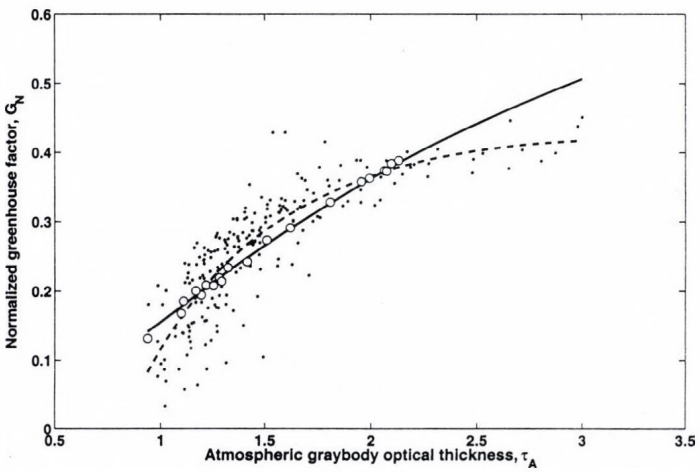

Fig. 25. Dependence of theoretical (solid line) and simulated (dots) normalized greenhouse factors on atmospheric graybody optical thickness. Open circles are the profiles closest to the radiative equilibrium. The dashed line was obtained by a second order polynomial fit to the dots.

These two facts imply that the dependence of G_N on the optical depth is a simple linear mapping of the $t_S(w)$ function. In other words, the local greenhouse effect does not follow the theoretical curve predicted by the radiative equilibrium, instead, it is controlled by thermodynamic and transport processes. However, the radiative equilibrium curve sets the global constraints. In case of an increase in the global average graybody optical thickness, the whole pattern will be shifted to the right along the equilibrium curve in a way that the new global average and the new radiative equilibrium optical thickness will be equal, assuring that the global radiative equilibrium

will hold. Perhaps, the structure of the pattern may change because of optical thickness perturbations have different relative effect at different latitudes. The magnitude of the shift (i.e., the new equilibrium optical thickness and surface temperature) is the function of the planetary albedo, solar constant, and the general dynamics of the system as well.

The derivative of Eq. (8) gives the sensitivity of the $\hat{g}$ parameter to the total optical thickness:

$$\hat{g}_S(\tau_A) = \frac{d\hat{g}(\tau_A)}{d\tau_A} = \frac{2\,(1-e^{-\tau_A})}{(e^{-\tau_A}+\tau_A+1)^2} = \hat{f}^2 A/2\,. \tag{9}$$

The variations of $\hat{g}(\tau_A)$ and $\hat{g}_S(\tau_A)$ functions for a wide range of τ_A are shown in *Fig. 26.* The values, corresponding to the global average optical thickness, $\tilde{\tau}_A = 1.86$, are marked with open and full circles.

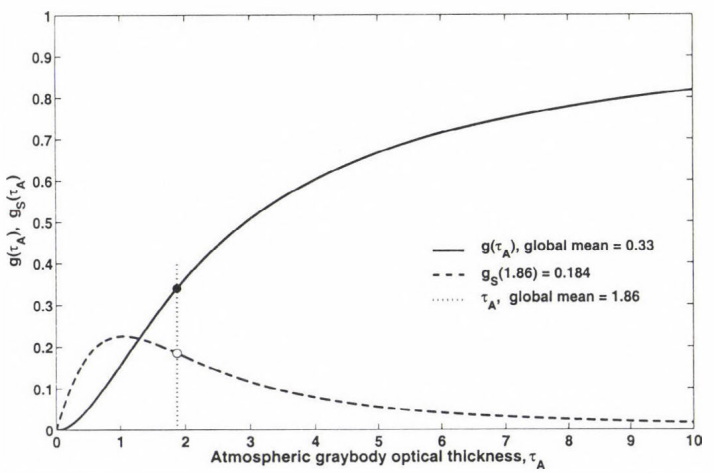

Fig. 26. Dependence of theoretical normalized greenhouse factor, Eq. (8), and its derivative, Eq. (9), on graybody optical thickness.

Using Eq. (9) one may easily estimate the initial tendency of the greenhouse temperature change due to greenhouse gas perturbations. To do this we need the value of $\hat{g}_S(\tilde{\tau}_A)$. From Eq. (9) the sensitivity is $\hat{g}_S(\tilde{\tau}_A) = 0.185$ per unit optical thickness. For example, a hypothetical CO_2 doubling would result in an increase of the global average $\tilde{\tau}_A$. To compute the increase in $\tilde{\tau}_A$ without much effort, global and zonal average atmospheric

profiles are needed. We computed the global average profile from the full TIGR dataset. To estimate the minimum and maximum expected temperature changes in cold and warm areas we also computed three zonal averages for the southern, tropical and northern latitudinal belts. The zonal belts were bounded by the following latitudes: -90, -42.2, 36.8 and 90 degrees (south is negative). The product of the optical depth perturbations with the sensitivity will give the expected changes in $\hat{g}$, from which, using the (unperturbed) *OLRs,* the surface temperature changes may be evaluated.

According to our estimate, a CO_2 doubling would rise the global average surface temperature by 0.48 K, corresponding to a global average primary greenhouse forcing of 2.53 W m^{-2}. The detailed results are included in *Table 6.*

Table 6. Effect of CO_2 volume mixing ratio perturbations. Current value is 366 ppmv

CO_2 perturbation	Change in τ_A (%)				Change in t_S (K)			
	Global	South	Tropic	North	Global	South	Tropic	North
0.0	-6.71	-19.4	-3.940	-16.90	-2.500	-5.070	-1.700	-4.720
0.5	-1.06	-2.17	-0.793	-1.93	-0.396	-0.579	-0.341	-0.547
2.0	1.29	2.25	1.060	2.02	0.482	0.601	0.455	0.573
10.0	6.16	9.14	5.350	8.29	2.290	2.450	2.290	2.360
100.0	22.30	30.00	20.00	27.50	8.200	8.100	8.430	7.840

We note, that the direct estimate using the right hand side of Eq. (5): $\Delta S_U = (dS_U / d\tau)\Delta\tau = A\,(\Delta\tau/2)\,OLR$ will give the same greenhouse forcing. For reference, our estimate is about 1.7 W m^{-2} (35%) less than the one published by Hansen (Table 1 on page 12754 in *Hansen et al.*, 1998). *Hansen et al.* (1998) used the correlated k-distribution method for the optical thickness calculations which compares well with LBL results. The reason of the relatively large differences in the greenhouse forcing must be the different method of relating the changes in the total optical thickness to the changes in the fluxes. Regarding the zonal temperature change estimates (in *Table 7*), once again we have to emphasize that keeping the zonal *OLR* as a constant (while changing the optical thickness) is not realistic. There exists only one overall constraint, and that is for the global average *OLR.*

An increase of 0.08 prcm in the global average w would result in the same temperature rise – or a decrease by the same amount could completely hide the greenhouse effect of the CO_2 doubling. Since the local and global variability of the water vapor column amount is more than a magnitude larger

on almost any practical time scale, the detection of the changes in the global and zonal greenhouse effect could be extremely difficult, and on local scale it is almost impossible. It is also obvious, that on a global scale, a strong direct $t_S \rightarrow \tau_A \rightarrow t_S$ feedback loop is not in effect in the Earth-atmosphere system.

The role of the water vapor in the Earth's atmosphere is very complex and is probably controlled by two major processes: the greenhouse effect and the redistribution of the system's heat energy by general circulation. As a result of these processes there are unique equilibrium meridional distributions for t_S and w. Obviously, the general circulation models (GCMs) are the adequate tools to predict those details. In any case, the decreasing tendency of the $\hat{g}_S(\tau_A)$curve above the unit optical thickness in *Fig. 26* and the negative temperature sensitivity of the $\hat{g}(\tau_A)$ function works against large positive feedback. It is interesting to note that in the clear atmosphere the CO_2 contribution to the total greenhouse effect is only about 9%, and an average atmosphere without CO_2 would be about 2.5 K colder. The above estimates are consistent with the wide range of predicted changes that can be found in the global warming literature.

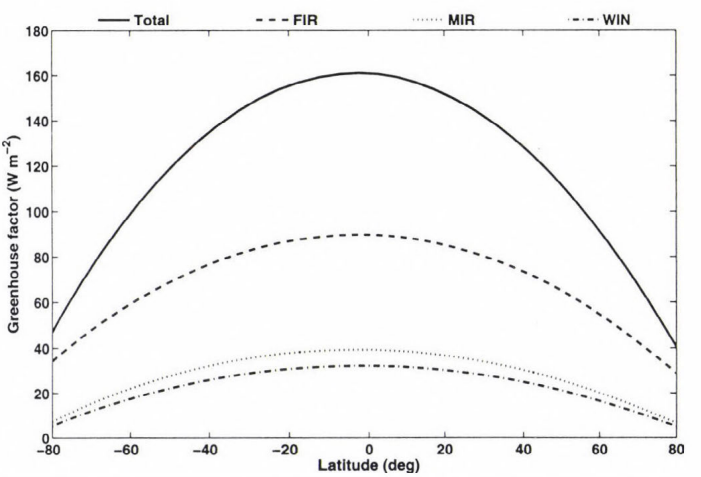

Fig. 27. Latitudinal dependence of the total and spectral greenhouse factors.

In *Fig. 27* the meridional variation of G is presented. Because of the direct dependence of G on the large meridional gradient in the surface temperature via S_U, and the larger sensitivity of the $\hat{g}_S(\tau_A)$ function at the polar regions, probably the first detection of the planetary greenhouse effect will be possible by the observations of the changes in the meridional gradient of the G factor. This is especially true for the FIR G component. Our data set

shows that the global average greenhouse factor is 131.8 W m^{-2}. The FIR contribution is 57%, and the shares of the MIR and WIN spectral ranges are 24% and 19%, respectively.

In *Fig. 28* the meridional distribution of the total and spectral G_N and the $\hat{g}(\tau_A)$ functions are plotted. The spectral G_N curves show the relative contributions to G_N from the FIR, MIR, and WIN regions. According to this figure, the total G_N is decreasing poleward from about 38% at the equatorial regions to about 15–20% at high latitudes. This behavior is obvious since decreasing water vapor content will increase the atmospheric infrared transparency almost everywhere in the longwave spectrum. The remarkably good agreement between the theoretically predicted greenhouse function and the simulated total normalized greenhouse factors further emphasize our earlier result, i.e., for zonal and global means the radiative equilibrium condition approximately holds.

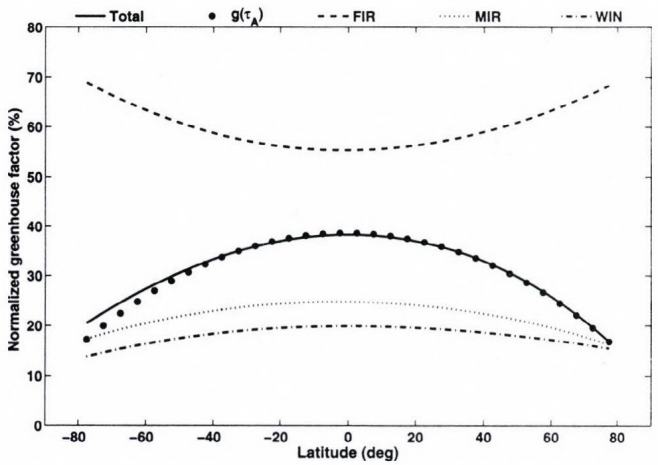

Fig. 28. Latitudinal distributions of the total and spectral normalized greenhouse factors. The full circles are computed by Eq. (8).

While the total G_N decreases poleward by about fifty percent, the far infrared contribution will increase from about 55% (of the total G_N) at the equatorial regions to 70% at +/–80 degrees latitudes. This increase, and the decrease of the MIR and WIN components, are due to the shift of the peak of the blackbody function toward the far infrared with decreasing temperature. The WIN G_N must also be affected by the ozone absorption, and theoretically, it should reflect the global average meridional distribution of the total ozone amount and the effective height of the ozone layer. Unfortunately, our data set does not contain sufficient information to explore these details.

4.3 Inverse terrestrial flux transmittance

The inverse terrestrial flux transmittance as another greenhouse parameter was introduced by *Stephens* and *Greenwald* (1991). Based on the functional relationship between I_T and G_N, this parameter does not contain any more information about the greenhouse effect than G_N and can not be related to the graybody atmospheric optical thickness in a simple way either. Theoretically I_T has a nonlinear relationship with the atmospheric graybody optical thickness:

$$I_T''(\tau_A) = \hat{f}^{-1} = \frac{1 + \tau_A + e^{-\tau_A}}{2}. \tag{10}$$

In *Fig. 29* the total I_T as the function of w is plotted with dots. According to *Stephens* and *Greenwald* (1991), the inverse terrestrial flux transmittance (I_T) may be related to the terrestrial graybody optical thickness of the atmosphere, and consequently, it is directly related to the atmospheric water vapor content. In *Stephens et al.* (1993) a linear relationship in the form of $I_T' = a + c * w$ was also assumed, where a and c are regression constants.

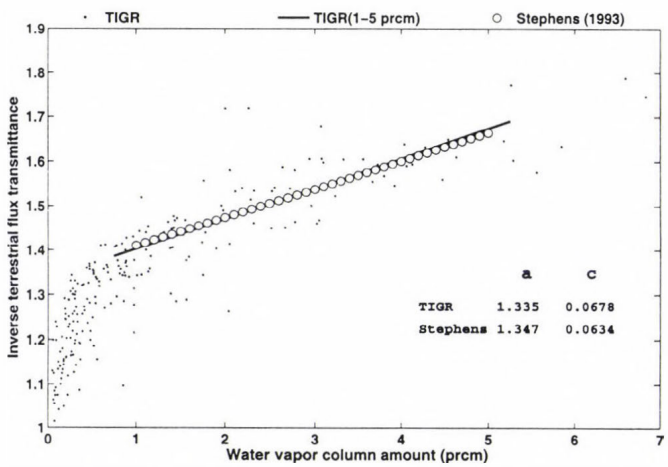

Fig. 29. Dependence of inverse terrestrial flux transmittance on water vapor column amount.

Based on satellite observations of *OLR*, w, and sea surface temperature, Stephens obtained the global annual mean distribution of I_T and computed the regression coefficients a and c for the year of 1989. His results are also displayed in *Fig. 29* as open circles. The thin solid line in the plot, which is representing the total simulated I_T, was obtained by a linear fit using the points

falling within the 1.0–5.0 prcm range. Regarding all the assumptions we made, and the accuracy of the satellite derived quantities in *Stephens et al.* (1993), this agreement is excellent, and at least in the 1–5 prcm range of w, the linear parameterization of the global greenhouse effect by the I'_T quantity looks adequate. However, the simple two-parameter characterization of the planetary greenhouse effect by I'_T for the full range of variability of w is not sufficient. Note, that Stephens curve fails to converge properly to 1.0 at low optical thickness, which is expected by the theoretical value I''_T. This tendency is reproduced pretty well by the simulated values.

4.4 Greenhouse temperature changes

The clear indication of the presence of the planetary greenhouse effect is the fact, that the global average surface temperature is much higher than the effective planetary temperature which is computed from the global average *OLR*. As we have shown in the introduction, using the ERBE data one may easily estimate the effective planetary temperature. The temperature difference, using an estimated 288 K global average surface temperature will result in an all-sky planetary greenhouse effect of 35 K. This corresponds to a global average $\hat{g}$ factor of 0.4.

In our data set t_E equals to 257.7 K, and t_G equals to 285.3 K. The temperature difference – we may call it clear-sky greenhouse temperature rise – is $dt_G = t_G - t_E = 27.91$ K, which is consistent with the theoretically predicted value: $dt_G = [OLR/(1-\hat{g})/\sigma]^{0.25} - t_G = 27.5$ K, and $\hat{g}$ is obtained from Eq. (8). The dependence of the local dt_G – computed as the difference of the local surface temperatures and effective temperatures – on the water vapor column amount is given in *Fig. 30.*

There are several possibilities to partition the dt_G function into the FIR, MIR, and WIN spectral regions. Here the dt_G components are weighted values with the corresponding spectral components of A_A. The dt_G dependence on w is non-linear, and at higher w, dt_G exhibits some saturation tendency, obviously related to the thermodynamic control of the column water amount. The greenhouse effect can be parameterized with sufficient accuracy via w, t_S, and O_3. If one insists on using simple formulas, Eq. (22) in *Table 4* reproduces the total greenhouse temperature rise with a correlation coefficient of 0.913. In this case the dependence on t_S and O_3 was ignored. The temperature differences computed from the downward and upward atmospheric emittances would produce practically the same results, therefore, we did not plot it in this figure.

The latitudinal variation of dt_G is presented in *Fig. 31*. The markers are the three degree zonal averages of the total dt_G. The major contributions to dt_G come from the FIR and WIN components, and the relatively sharp peak at the tropical area is caused by the WIN component. The much smaller latitudinal changes in the FIR and MIR components could be related to the same compensation mechanism affecting the FIR and MIR *OLR*s.

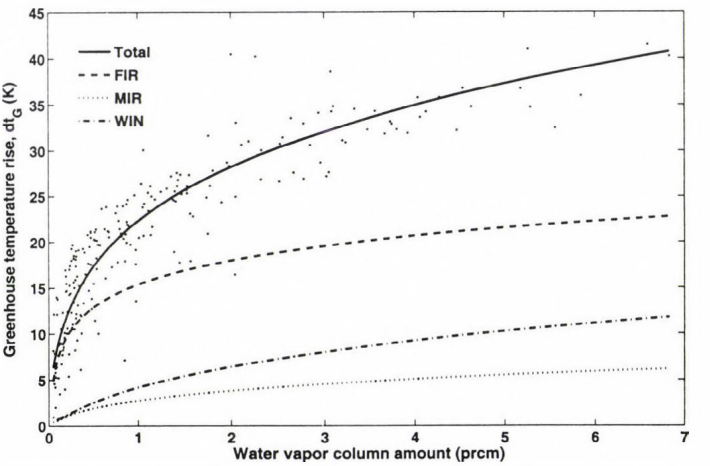

Fig. 30. Dependence of greenhouse temperature rise on water vapor column amount.

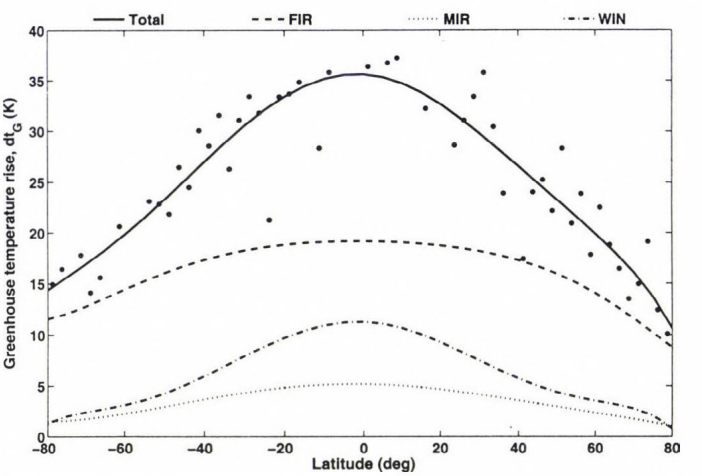

Fig. 31. Latitudinal variation of the greenhouse temperature rise, dt_G.

There are further possibilities to express the magnitude of the greenhouse effect for example, via the total absorbed flux density of the atmosphere, $A_A = S_U - S_T = S_U\ A$, or the downward atmospheric emittance E_D, see *Fig. 20*. In *Fig. 32*, we plot the quantity of $dt_A = t_S - \hat{t}_A$, as the function of w. Here $\hat{t}_A$ may be called as the clear-sky brightness temperature, computed from the total absorbed flux density using the Stefan-Boltzmann law. This figure expresses the fact that with increasing w the surface is getting closer to the radiative equilibrium with the atmosphere. All over the range of w the FIR spectral range is the major contributor to the total dt_A.

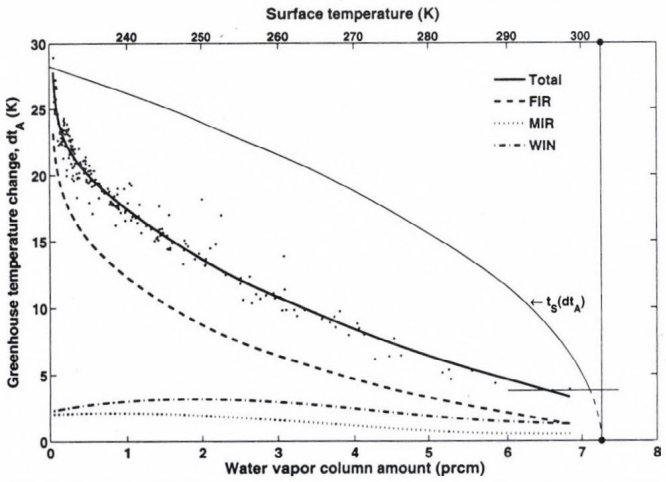

Fig. 32. Dependence of greenhouse temperature change, dt_A, on water vapor column amount and surface temperature.

Just like in the case of the dt_G, these curves are also showing some tendency for saturation at larger w. This tendency, as we mentioned already, is related to the direct thermodynamic control of the water vapor column amount. In *Fig. 32* the $t_S(dt_A)$ function is also plotted with a thin line. The extrapolation of this curve toward the dt_A = 0 line (dashed part of the curve) will point to the critical values of t_S and w, where the radiative cooling of the surface stops. Based on our data set, these values are 303.8 K and 7.38 prcm, respectively. According to the minimum value of dt_A – which is 3.77 K, and marked with a short horizontal line – such situation in the Earth's atmosphere is not likely to happen. Before reaching the above limits, the more efficient thermodynamic and transport processes will take over the re-distribution of the local surface heat energy and the water vapor amount.

None of the above discussed greenhouse parameters are better than the other. Which one to use largely depends on the available data and the nature of the radiative transfer problem at hand. It must be clear, that the greenhouse effect is a large scale phenomenon which requires the existence of the radiative equilibrium as a constraint, both for the temperature profile and the *OLR*. Eqs. (1)–(10) are only valid under the radiative equilibrium condition. Our results show that for global and zonal averages this condition approximately holds. The chances are very little to randomly select an individual vertical air column with its temperature profile in IR radiative equilibrium and measure the greenhouse effect.

Unfortunately, within the frame of this paper we could not go into the full mathematical details of the solution of the Schwazschild-Milne equations and the mathematical proofs of the new equations.

5. Conclusions

Besides the number of interesting details, the most significant result of this research was to establish a qualitative picture of the clear-sky spectral radiative properties of the Earth-atmosphere system in the three most important spectral regions. Several simple and accurate formulas of different physical quantities have been developed for direct use in practical applications. The basic tendency of the meridional variations of the FIR, MIR, and WIN spectral components were derived. We derived fundamental theoretical relationships that strongly supported the simulation results on the H_2O and CO_2 greenhouse effects. These results could be valuable contributions to the general global picture given by *Hansen* (1998), *Paltridge* and *Platt* (1976), or *Peixoto* and *Oort* (1992), or by several others who were not mentioned here. The application of our transfer and greenhouse functions in GCM climate simulations may also improve our understanding of the greenhouse effect in the Earth's atmosphere.

Equations related to the semi-infinite atmospheric model were replaced with new relationships valid for the semi-transparent atmosphere. With the help of the newly introduced transfer and greenhouse functions we established the connection between the theoretical and empirical greenhouse parameters. Probably the most important consequence of the semi-transparent atmospheric model is the significant reduction in the expected response in the surface upward flux density to greenhouse gas perturbations.

Obviously, the presented results have their limitations. The most significant one is related to the temperature profile data base. In some latitudinal belts we had rather few soundings, therefore, it is difficult to set up

selection procedures to obtain statistically consistent data sets for each latitudinal belts. There are virtually unlimited possibilities in increasing the complexity of such simulations by involving more atmospheric and surface parameters. The scientific community dealing with the present and future of the greenhouse effect of the Earth's atmosphere would certainly welcome such extensions of this kind of research. A similar study which deals with the cloud effect is also desirable.

Using an LBL code for the radiative transfer computations was also crucial. The fine details of the transitions of the flux transmittances from the opaque to the transparent spectral regions, especially at higher altitudes, can only be traced with correct mathematical representation of the infrared radiative transfer. Although the speed of computers are improving, the computational burden of doing such simulations on much larger data sets could be a concern.

The presented results in the FIR spectral range are awaiting the confirmation by direct observations. Apparently in the FIR region there is a kind of spectral compensation in effect which prevents the FIR *OLR* to dramatically respond to the poleward temperature decrease. However, statements on the variability of the FIR *OLR* must be supported by a solid FIR climatology, which is based on direct observations. The predicted meridional variation in the total and spectral transmitted flux densities should also be supported by observations. The role of the FIR and WIN spectral regions in forming the greenhouse temperature rise is obvious. One should not forget that the boundaries of the spectral ranges are unique, and changing these boundaries will alter the contributions of the different spectral components. The most critical wave number is the one which separates FIR and WIN regions.

In general, the qualitative picture given above must be validated against direct satellite measurements especially in the FIR spectral range. The first opportunity to gather satellite measured fluxes in the FIR spectral range has just arrived. The utilization of the differences of the coincidental flux measurements from the Terra and Aqua satellites will give us the first measured global radiative fluxes in this important spectral region.

Acknowledgements—This research was supported by the NASA Science Mission Directorate through the EOS project, (contract No. NAS1-02058). Support was also received from *M. Kurylo, D. Anderson,* and *H. Maring* at NASA HQ. We are very grateful to *S. Gupta* at AS&M for his helpful discussions regarding the scientific and technical details of the manuscript.

References

Brindley, H.E. and *Harries, J.E.*, 1997: The impact of far infra-red absorption on greenhouse forcing: sensitivity studies at high spectral resolution. In *IRS'96 Current Problems in Atmospheric Radiative Transfer*. Deepak pub., 981-984.

Brutsaert, W., 1975: On a derivable formula for longwave radiation from clear skies. *Water Resour. Res. 11*, 742-744.

Chedin, A. and *Scott, N. A.*, 1983: *The Improved Initialization Inversion Procedure*. Laboratoire de meteorologie dynamique. Centre National de la Recherche Scientifique, No. 117.

Collins, II, G.W., 2003: The *Fundamentals of Stellar Astrophysics. Part II. Stellar Atmospheres*. WEB edition.

COVE, 2003: COVE Time Synchronized Monthly Archive Files, http://www-svg.larc.nasa.gov.

ERBE, 2004: ERBE Monthly Scanner Data Product. NASA Langley Research Center, Langley DAAC User and Data Services, userserv@eosdis.larc.nasa.gov.

Goody, R.M. and *Yung, Y.L.*, 1989: *Atmospheric Radiation. Theoretical Basis*. Oxford University Press, Inc.

Gupta, S.K., 1989: A parameterization for longwave surface radiation from Sun-synchronous satellite data. *J. Climate 2*, 305-319.

Gupta, S.K., Darnell, W.L., and *Wilber, A.C.*, 1992: A parameterization for longwave surface radiation from satellite data: recent improvements. *J. Appl. Meteorol. 31*, 1361-1367.

Hansen, J.E., Sato, M., Lacis, A., Ruedy, R., Tegen, I., and *Matthews, E.*, 1998: Climate forcings in the industrial era. *Proc. Natl. Acad. Sci. USA, Vol. 95*, 12753-12758.

HITRAN2K, 2002; http://cfa-www.Harvard.edu/HITRAN/hitrandata.

Husson, N., Bonnet, B., Chedin, A., Scott, N., Chursin, A.A., Golovko, V.F., and *Tyuterev, V.G.*, 1994: The GEISA databank in 1993: a PC/AT compatible computers' new version. *J. Quant. Spectrosc. Ra. 52*, 425-438.

Idso, S.B., 1981: A set of equations for full spectrum and 8-14 μ and 10.5-12.5 μ thermal radiation from cloudless skies. *Water Resour. Res. 17*, 295-304.

Kiehl, J.T. and *Trenberth, K.E.*, 1997: Earth's annual global mean energy budget. *B. Am. Meteorol. Soc. 78*, 197-208.

Kratz, D.P., Mlynczak, M.G., Mertens, C.J., Brindley, H., Gordley, L.L., Martin-Torres, J., Miskolczi, F.M., and *Turner, D.D.*, 2005: An inter-comparison of far-infrared line-by-line radiative transfer models. *J. Quant. Spectrosc. Ra. 90*, 323-341.

Miskolczi, F., Bonzagni, M., and *Guzzi, R.*, 1990: High-resolution atmospheric radiance-transmittance code (HARTCODE). In *Meteorology and Evironmental Sciences: Proc. of the Course on Physical Climatology and Meteorology for Environmental Application*. World Scientific Publ. Co. Inc., Singapore, 743-790.

Miskolczi, F. and *Rizzi, R.*, 1998: High accuracy skin temperature retrieval using spectral measurements of multi-channel imagers. *International Radiation Symposium 1998*, Madison, Wisconsin, USA.

Paltridge, G.W. and *Platt, C.M.*, 1976: *Radiative Processes in Meteorology and Climatology*. Elsevier Scientific Publishing Company.

Peixoto, J.P. and *Oort, A.H.*, 1992: *Physics of Climate*. American Institute of Physics, NewYork.

Raval, A. and *Ramanathan, V.*, 1989: Observational determination of the greenhouse effect. *Nature 342*.

Rizzi, R., Matricardi, M., and *Miskolczi, F.*, 2002: On the simulation of up-looking and down-looking high-resolution radiance spectra using two different radiative transfer models. *Appl. Optics 41*, 940-956.

Rodriguez, R., Jucks, K.W., Lacome, N., Blanquest, G., Valrand, J., Traub, W.A., Khalil, B., LeDoucent, R., Valentin, A., Camy-Peyret, C., Bonamy, L., and *Hartmann J.M.*, 1999: Model, software, and data-base for computation of line-mixing effects in infrared Q branches of atmospheric CO_2. I. Symmetric isotopomers. *J. Quant. Spectrosc. Ra. 61*, 153-184.

Rothman L.S., Rinsland, C.P., Goldman, A., Massie, T., Edwards, D.P., Flaud, J-M., Perrin, A., Camy-Peyret, C., Dana, V., Mandin, J-Y., Schroeder, J., Cann, A., Gamache, R.R., Wattson, R.B., Yoshio, K., Chance, K.V., Jucks, K.W., Brown, L.R., Nemtchinov, V., and *Varansi, P.,* 1998: The HITRAN molecular spectroscopic database and HAWKS (HITRAN atmospheric workstation): 1996 edition. *J. Quant. Spectrosc. Ra. 60,* 665-710.

Rozanov, A., 2001: *Modeling of Radiative Transfer through a Spherical Planetary Atmosphere: Application to Atmospheric Trace Gases Retrieval from Occultation- and Limb-measurements in UV-Vis-NIR.* Dissertation, Institut für Umweltphysik, Universität Bremen.

Rutten, R.J., 2000: *Radiative Transfer in Stellar Atmospheres.* Lecture notes, Utrecht University. 7th edition.

Schneider, E.K., Kirtman, B.P., and *Lindzen, R.S.,* 1999: Tropospheric water vapor and climate sensitivity. *J. Atmos. Sci. 56,* 1650.

Stephens, G.L. and *Greenwald, T.J.,* 1991: The Earth's radiation budget and its relation to atmospheric hydrology. 1. Observations of the clear-sky greenhouse effect. *J. Geophys. Res. 96,* No. D8, 15311-15324.

Stephens, G.L., Slingo, A., and *Webb, M.,* 1993: On measuring the greenhouse effect of Earth. *NATO ASI Series, Vol. 19,* 396-417.

Tobin, D.C., Best, F.A., Brown, P.D., Dedecker, R.G., Ellingson, R.G., Garcia, R.K., Howell, H.B., Knuteson, R.O., Mlawer, E.J., Revercomb, H.E., Short, J.F., Van Delst, P.F.W., and *Walden, V.P.,* 1999: Down-welling spectral radiance observations at the SHEBA ice station: Water vapor continuum measurements from 17 to 26 μm. *J. Geophys. Res. 104,* No. D2, 2081-2092.

Tuzet, A., 1990: A simple method for estimating downward longwave radiation from surface and satellite data by clear skies. *Int. J. Remote Sens. 11,* 125-131.

Vonder Haar, T., 1986: WCP 115, *WMO ITD,* No. 109, pp. 144.

IDŐJÁRÁS

Quarterly Journal of the Hungarian Meteorological Service
Vol. 108, No. 4, October–December 2004, pp. 253–263

Influence of different sensor positions on leaf wetness duration measurements and their effect on the simulation of grapevine downy mildew (*Plasmopara viticola*)

A. Dalla Marta[1*] S. Orlandini[1], M. Ghironi[1] and F. Sabatini[2]

[1]*Department of Agronomy and Land Management, University of Florence, Piazzale delle Cascine, 18 - 50144 Firenze, Italy*
E-mails: anna.dallamarta@unifi.it; simone.orlandini@unifi.it

[2]*Institute of Biometeorology, National Research Council, Via Caproni, 8 – 50135 Firenze, Italy; E-mail: f.sabatini@ibimet.cnr.it*

(Manuscript received February 6, 2004; in final form September 13, 2004)

Abstract—Leaf wetness duration (LWD) is one of the most important variables responsible for development of plant diseases. Thus, its measurement represents the basis for disease forecasting models, developed and applied with the aim of timing fungicide application, for avoiding environmental damages, waste of resources, and money losses. Despite of its importance, there is no widely accepted standard for LWD measurement, and the different measurement principles, sensor designs, and installation positions are responsible for different results affecting the quality of model simulations. For this reason, four leaf wetness sensors were mounted in a vineyard in two different positions, at one quarter and three quarters of the canopy height, and in two expositions, east and west. Measured LWD was analyzed and compared with visual inspections conducted during the experiment in order to establish the performance obtainable from different sensor positionings, and to asses their impact on the simulation of grapevine downy mildew (*Plasmopara viticola*).

Key-words: disease forecasting, simulation modeling, *Vitis vinifera*.

1. Introduction

In every epidemic system, climatic factors play a role of major concern, affecting the parasite and host development, which, in turn, widely controls the whole evolution of the infective processes. In particular, the factor "water" is really important in many phases of disease development. The presence of free water on a plant surface often represents an indispensable condition for the beginning of the contamination phase (*Egger et al.*, 1996). The exigency of

* Corresponding author

water, in terms of leaf wetness duration (LWD), varies from one pathogen to another, therefore, its knowledge becomes fundamental for plant disease forecasting and, consequently, for crop protection.

Pathogen behavior has been classified in relation with its requirements of leaf wetness for the infection development (*Huber* and *Gillespie*, 1992). Five categories have been identified, starting from pathogens strictly dependent on free water (for example, the Oomycetes) to pathogens which have a minimum or no LWD requirement as powdery mildew (*Erysiphe necator*) or, in some cases, which are obstructed by the presence of water on host tissues. The importance of LWD is confirmed by its use as driving variable of many epidemiological models for the simulation and forecasting of many diseases (*Hoppmann*, 1996). Grapevine downy mildew (*Plasmopara viticola*), apple scab (*Venturia inaequalis*), cercospora leaf spot (*Cercospora beticola*), wheat ear rot (*Fusarium graminearum*), etc., are among the most studied diseases for which accurate simulation models using LWD are available (*Hoppman*, 1996). In the last years, in fact, development of simulation models based on agrometeorological variables became more and more important, especially in the field of phytosanitary defence, with the aims to improve the production quality, reduce the costs, and increase the environment safeguarding (*Campbell* and *Madden*, 1990; *Seem et al.*, 2000). On the other hand, at present not every meteorological variable is measured and available with enough accuracy and spatial and temporal resolution to be successfully used by such agrometeorological models (*Maracchi*, 2003).

The main problem is that LWD is not always observed on a routine basis, and for this reason, there is a lack of agreement about a standard sensor design and protocol for the use of sensors. In addition, as most of the sensors measure LWD indirectly and have different physical properties from leaves, sensors require calibration to represent a specific crop (*Getz*, 1991). A particular care is needed to sensor positioning that has to reflect the leaf exposition and inclination as much as possible (*Gozzini et al.*, 1996). Finally, the variable itself has been poorly defined, so it can be said that the methodology of LWD estimation is in a state of infancy (*Magarey*, 1999).

The differences pointed out by many authors between the real and measured LWD (*Caprara* and *Veronesi*, 1992) as well as among measurements carried on by different sensors (*Egger* and *Marinelli*, 1995), had lead to the exigency to analyze the possible influences, that different methods of LWD assessment could have on the forecasting of pathogens attack.

On these basis, the aim of this work was to compare different LWD sensor positionings in the vineyard, and to establish how these different measurements could affect the output of a model that simulates grapevine downy mildew infections using agrometeorological variables.

2. Materials and methods

The experiment was conducted in the Paretaio vineyard, located in Tuscany (central part of Italy), in the northern part of Chianti region, in the period of April–September 2003. Grapevine (*Vitis vinifera*) were cordon trained and spur pruned, rows were north-south oriented, and the spacing was 1.0 m in the rows and 3.0 m between the rows. The canopy was developed between 90 and 210 cm above the ground (*Fig. 1*).

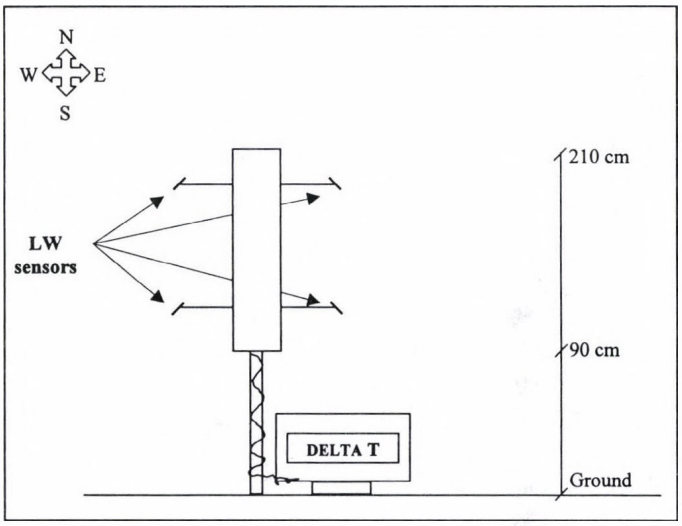

Fig. 1. Scheme of grape canopy and sensor positions connected with the data logger.

Leaf wetness data were collected in 3 different ways: by a single sensor installed on a standard weather station placed near the vineyard; by 4 sensors placed at canopy level; and by visual observations. The sensors (S.W. and W.F. Burrage, Ashford, Kent, U.K.) used in this work were low consumption electronic transducers operating on the basis of resistance variations that occurs in the presence of water. The sensible part of the transducer is constituted by a flat surface made by 3 graphite electrodes separated by a waterproof resin with rough surface in order to increase the active area. The transducer active surface is made by graphite and plastic, then all the complex results to be chemically inert toward the components of phytopathological treatments and organic residuals. The sensor dimensions were 450 mm^2 of active area, 150 mm of length, and 20 mm of diameter. The transducer furnishes a 0-1 logical signal: in fact the presence of water on the active

surface affects the system resistivity and the out signal varies between 0 (dry) and 1 (wet). A drop of distilled water of 1 mm of diameter is sufficient for varying the condition from dry to wet. The sensor response time is lower then 0.5 seconds.

The 4 sensors at canopy level were placed at two different exposures, east and west, and two different heights, one quarter (110 cm above the ground) and three quarters (180 cm above the ground) of the canopy height. Sensors were mounted with an inclination angle of 45° to imitate grapevine leaves position. They were connected with a data logger (Delta-T mod. DL2, Burwell, Cambridge, UK), and the data were recorded with 10 minutes time resolution (*Fig. 1*).

The single sensor was part of the equipment of an agrometeorological station placed just outside of the vineyard. The sensor was exposed to north and mounted with an inclination of 45°. The station was also fitted for air temperature (°C) (Vaisala HMP45, Helsinki, Finland), relative humidity (%) (Vaisala HMP45, Helsinki, Finland), and precipitation (mm) (RGB1, Institute of Hydrology, Wallingford, UK) measurements to collect all the input data required by the epidemiological model. All the sensors were connected to a data logger (Delta-T mod. DL2, Burwell, Cambridge, UK), and in this case the data also were recorded every 10 minutes.

The technique for visual observation of LWD has required some months to be set up. The presence of a layer of water on a leaf, in fact, is clearly visible, the difficulty is to determine the percentage of surface concerned. For this reason two observers were skilled with a series of exercises for determining the percentage of wet surface in special pictures of leaves. At the end of the training the error committed by the two observers was less than 3%.

The visual observations were made in correspondence to the sensor positions in the canopy and the data were recorded every 20 minutes starting from 10 p.m. until the complete surface wetness at night, and from sunrise to the complete dew depletion in the morning. The observations took place during 12 rainless nights and were made on 40 leaves (20 eastward and 20 westward, 10 for each canopy height). The observations were carried on with the help of some powerful electric torches to determine the percentage of leaf surface covered by water, and the threshold for considering a whole leaf as wet was 10% of its surface. LWD beginning and ending were recorded when at least 50% of the sampling was wet or dry. These data were taken separately to compare the visual observations to the sensor measurements, while to compare the observations and sensor measurements to the data recorded by the agrometeorological station outside the vineyard, the 4 positions data were considered together as a single set and LWD was considered to begin and finish, when at least 3 of the 4 positions were wet or dry.

To compare sensor measurements with visual observations, statistical analyses were carried out in two different ways; the first control was made among visual observations, the set of inside canopy sensors, and the outside sensor to compare the proportion of hours correctly classified as wet and dry using a dichotomous categorical verification (*Wilks*, 1995). In this case the statistical indices used were: "Probability of Detection" (POD) representing the probability to measure correctly the observed event; "Critical Success Index" (CSI) representing the ability of the measure to discriminate between yes and no observations; "Bias" that is the ratio of the number of yes measures to the number of yes observations, and it is an index of over- or under-estimation of LWD.

The second control was made by calculating the statistic indices of mean absolute error (MAE), root mean squared error (RMSE), and mean real error (MRE) for the time of wetting and drying and for the length of individual wetness periods both visually observed and recorded by sensors in each position.

Afterwards, LWD data measured at canopy level and outside the vineyard were used to feed the grapevine downy mildew simulation model Plasmo. The mathematical model Plasmo has the purpose to estimate the severity (%) of the grapevine downy mildew disease development through the principal biological stages: primary infection, loss of vitality, sporulation, infection, and incubation (*Orlandini* and *Rosa*, 1997; *Rosa* and *Orlandini*, 1997). Besides LWD, the corresponding meteorological inputs required at hourly interval (temperature (°C), relative humidity (%), precipitation (mm)) were measured by the weather station located outside the vineyard.

In order to compare the simulation model performances obtained using different LWD data, visual surveys of the disease were made during the season in the Paretaio vineyard. The observations were made by two skilled technicians every month from May to September in samples of 100 leaves each randomly chosen in untreated plots of the vineyard. Differences between downy mildew simulations and observations were statistically analyzed by calculating MAE, RME, and RMSE values.

3. Results

3.1 Leaf wetness observations in relation to sensor position

A comparison between the set of sensors placed in the canopy and the set of observations showed a tendency of sensors to underestimate LWD, with a bias of 0.64 (*Table 1*). On the contrary, comparing both the set of observations and

the set of inside canopy sensors with the outside canopy, this latter always overestimated the phenomenon as demonstrated by the bias values, 1.60 and 1.56 for inside canopy sensors and observations, respectively (*Table 1*). POD and CSI values showed that the outside canopy sensor gave the best performance; its measurements, compared with observations, led to a POD of 0.93 with a CSI of 0.57, while the inside canopy sensor measurements gave the definitely worst performance, with a POD of 0.50 and CSI of 0.44. The comparison between inside canopy and outside canopy sensors led to an intermediate result (POD 0.91 and CSI 0.54) (*Table 1*).

Table 1. Comparison of proportions of hours that are correctly classified as wet and dry. Legend: POD = Probability of Detection; CSI = Critical Success Index. Observed is referred to the visual observations, Inside and Outside are referred to the set of inside and outside canopy sensors, respectively

	POD	CSI	BIAS
Observed-Inside	0.50	0.44	0.64
Observed-Outside	0.93	0.57	1.56
Inside-Outside	0.91	0.54	1.60

With regard to the measurements of dew onset, depletion, and duration, the comparative analysis could be divided into two parts. The first one compared the 4 different positions of inside canopy sensors with the same 4 positions of visual inspection, and the second one compared the set of inside canopy sensors and observations with the outside canopy sensor.

Table 2. Comparison between the 4 positions of inside canopy sensors and the respective visual observations. Values are expressed in hours. Legend: MRE = Mean Real Error; RMSE = Root Mean Squared Error; MAE = Mean Absolute Error

	Starting			Ending			Duration		
	MRE	RMSE	MAE	MRE	RMSE	MAE	MRE	RMSE	MAE
Up east	0.02	1.22	1.02	0.17	0.30	0.19	0.11	2.01	1.23
Down east	0.08	0.54	0.29	0.20	0.35	0.20	0.45	3.13	2.10
Up west	0.00	0.53	0.33	0.22	0.38	0.22	0.23	3.16	1.16
Down west	0.04	2.32	1.35	-0.03	0.26	0.17	0.59	3.30	2.44

When comparing the 4 different sensor positions and observations (*Table 2*), it could be noticed that for up east and west positions leaf wetness duration errors were evidently lower than the respective down positions. MAE values

were 1.23 and 1.16 hours, respectively, while those for down positions were 2.10 and 2.44 hours. For leaf wetness depletion the errors are really small for every considered position, with a maximum MAE of 22 minutes and minimum of 17.

When the 4 positions were averaged and considered together for analyzing the outside canopy sensor performance, the errors were generally increased in comparison with the sensors considered singularly (*Table 3*). For every considered phase (onset, duration, and depletion) the inside canopy sensors made lower error than the set of the outside canopy sensors that had a clear tendency to overestimate LWD (*Table 3*).

Table 3. Comparison between the visual observation, set of inside canopy sensors and outside sensor. Values are expressed in hours. Legend: MRE = Mean Real Error; RMSE = Root Mean Squared Error; MAE = Mean Absolute Error. Inside and Outside are referred to the set of inside and outside canopy sensors, respectively

	Starting			Ending			Duration		
	MRE	**RMSE**	**MAE**	**MRE**	**RMSE**	**MAE**	**MRE**	**RMSE**	**MAE**
Observed-Inside	0.06	1.00	0.32	-0.52	1.39	1.04	1.06	3.08	1.56
Observed-Outside	-1.05	2.00	1.35	-2.11	1.10	1.54	-2.15	3.03	2.23

3.2 Sensitivity of simulation model Plasmo to different LWD measurements

Plasmo was applied for the Paretaio vineyard during the season April–September 2003. The model was fed with the agrometeorological data collected by weather station outside the vineyard using the data collected by the set of inside canopy sensors with the 4 separate positions and by the sensor outside the vineyard as LWD input data. The model outputs (i.e., simulated infection periods) were then compared with the real infection data.

In general, all the simulations gave a satisfactory performance: in fact, the severity observed at the end of the season was 4.69% and the simulation ranged between 5.13% and 3.29% (*Table 4*). Thus, the low level of errors was also determined by the low infection pressure of grapevine downy mildew, because climatic conditions of 2003 were not favorable for the disease development. During the period June–August, in fact, mean temperature was very high (26°C), the amount of leaf wetness due to dew were very small (184 hours), and rain was low (86 mm). Nevertheless, some considerations have to be pointed out. For example, the comparison between the severity simulated with LWD measured by the sensor placed outside the vineyard, and the set of inside canopy sensors (*Fig. 2*), respectively, showed a slight overestimation and

underestimation of the disease as regards the final observed value. In fact, the observed severity was 4.69%, the outside canopy sensor measurements led to a value of 5.13% while the severity simulated using the inside canopy sensor measurements was 3.35% (*Table 4*).

Table 4. Severity of downy mildew by the end of the season and number of infection periods simulated using the different leaf wetness measurements. Legend: MRE = Mean Real Error; MAE = Mean Absolute Error; RMSE = Root Mean Squared Error. Errors are calculated for the whole season. Inside and Outside are referred to the set of inside and to the outside canopy sensors respectively

Sensor	Severity (%)	Number of infections	MRE	MAE	RMSE
Outside	5.13	8	-0.05	0.69	0.80
Inside	3.35	5	0.94	0.94	1.28
Up east	3.29	5	0.96	0.96	1.29
Down east	3.77	6	0.69	0.79	1.07
Up west	4.95	8	0.00	0.64	0.79
Down west	4.01	6	0.58	0.74	0.98
Observed	4.69	-	-	-	-

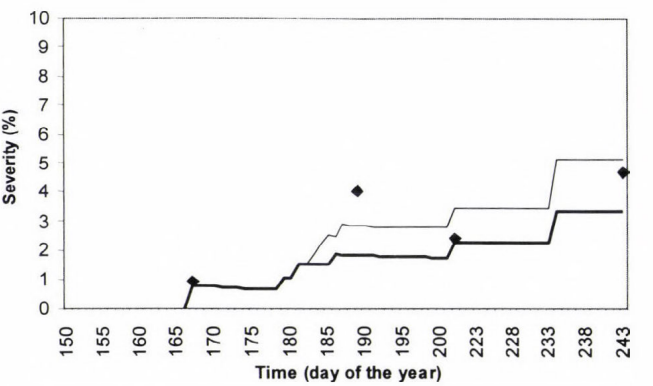

Fig. 2. Downy mildew severity observed (dots), simulated with leaf wetness measured by the outside canopy sensor (thin line) and set of inside canopy sensors (bold line).

A further analysis was carried out by separating the inside canopy sensors according to their single position (*Fig. 3*). It could be noticed that the up west position gave the best result leading to a really unimportant overestimation of the final severity (4.95%) (*Table 4*).

The LWD measurements obtained from the other sensor positions, however, have caused a more or less evident underestimation of downy mildew attack, clearly showed by the positive figures of MRE. Among these, the down west sensor position generated the lowest error (0.58), while the up east generated the highest one (0.96) (*Table 4*). Then, downy mildew severity was best simulated by using the measurements of sensors placed in the west side of the canopy.

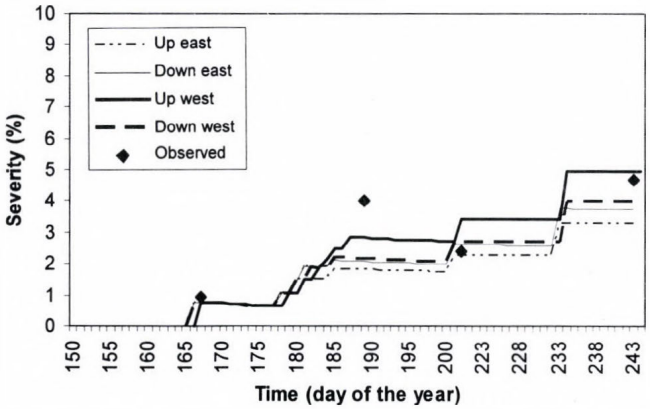

Fig. 3. Downy mildew severity observed (dots) and simulated with leaf wetness measured by the inside canopy sensors.

4. Discussion and conclusions

The analysis of the results highlights, as expected, that the outside canopy sensor always records a longer LWD as compared to the inside canopy sensors. This difference in the amount of wet hours recorded by the instruments was probably due to the fact, that sensors placed directly within the grape canopy were disturbed by the canopy itself. The sensors inside the canopy, in fact, were partly covered by the foliage that, intercepting the sky long wave radiation during the night, causes a slower cooling of the sensor that, in turn, could be traduced in a slower process of dew deposition on its active surface. This idea, in part, is strengthened by the lower error values given by both the upper positions of sensors for LWD. Some previous studies (*Weiss* and *Lukens*., 1981, *Jacobs et al.*, 1990; *Potratz et al.*, 1994) suggested that the best site for a sensor is just below the top of the canopy (approximately at the three quarters of the canopy height) but exposed to the sky radiation, because this position has the greatest surface wetness and, at the same time, some protection from the wind and early morning sun is given.

Looking at the errors made by each single sensor placed within the canopy and set of 4 sensors considered together, this latter raised an averaged value. This result is supported by previous works (*Penrose* and *Nicol*, 1996; *Magarey*, 1999), which indicated that a single sensor, as generally used in standard weather stations, can lead to an imprecise measurement. There are indications that 3 sensors should be used for a mean determination.

According to the previous indications, results of this work suggested that for a good LWD data quality, the best choice would be the positioning of at least 3 LWD sensors placed within the grape canopy. Otherwise, when such a set of sensors is not available, to avoid the variability due to the canopy effect, the choice has to be addressed to the use of a single sensor placed outside the vineyard. Anyway, the required precision of LWD data depends on their further use. In fact, for forecasting plant diseases related to LWD, in order to plan opportunely the crop protection, overestimation of LWD most of the time is more suitable than a slight underestimation, because LWD is a threshold parameter and the model starts to simulate the infections from a certain amount of LW hours. Then, LWD underestimation could induce the model not to detect the disease or to underestimate its severity which, in turn, may induce farmers to avoid treatments which are necessary, because the disease becomes aggressive.

As regards to the simulation of downy mildew attack, it can be safely said that the model was affected by the different LWD measurements. Considering the comparison between the outside canopy sensor, which overestimated LWD, and the set of inside canopy sensors, this latter produced a too low final severity in comparison to the observations (it raised only 3.35%, while the real severity was 4.69%). The outside sensor, determining a slight overestimation of severity, can be considered suitable also regarding farmer requirements.

In general, it can be concluded that LWD sensors do not always supply a precise datum and the precision varies depending on the sensor placement. Furthermore, the need of data precision mainly depend on their further utilization. Disease forecast models, related to LWD, are used to time the application of fungicides and provide effective disease management with the potential to reduce the number of total applications (*Russo, 2000*). These models are then really important in order to carry out a more sustainable and thoughtful agriculture, in respect of the environmental safeguard principles to obtain a safe production of high quality. Because of this extreme importance, besides the need of a suitable standard for sensor design and a protocol for their use, it is necessary to study alternative ways. In particular, the set up of mathematical models, based on agrometeorological variables for the simulation of LWD is a suitable response to the lack of sensor reliability. Moreover, the developments in remote sensing techniques, both with satellite and radar, could

bring a really useful contribution to the assessment of LWD with the advantage to give an output already spatially distributed on the studied territory. The integration of sensors, modeling, and remote sensing, then, could represent the more suitable way for obtaining precise and reliable LWD data.

References

Campbell, C.L. and *Madden, L.V.*, 1990: *Introduction to Plant Disease Epidemiology*. Wiley, New York.

Caprara, C. and *Veronesi, G.*, 1992: La misura dei parametri meteoclimatici in fitoiatria: la bagnatura fogliare. *Informatore Fitopatologico 4*, 29-32.

Egger, E. and *Marinelli, E.*, 1995: Confronto tra diversi sensori ed un metodo per la stima della bagnatura fogliare. *Informatore Fitopatologico 45*, 48-54.

Egger, E., Marinelli, E., and *D'Arcangelo, M.*, 1996: Influenza di diversi metodi per la stima della bagnatura fogliare sulla previsione degli attacchi di peronospora e muffa grigia sulla vite. *Informatore Fitopatologico 3*, 67-61.

Getz, R.R., 1991: Report on the measurement of leaf wetness. *WMO Publication*, No. 2, Geneva, Shwitzerland.

Gozzini, B., Orlandini, S., and *Seghi, L.*, 1996: Influenza della vegetazione e dell'orientamento del sensore sulla rilevazione della bagnatura fogliare. *Informatore Fitopatologico 4*, 55-59.

Hoppmann, D., 1996: *Agarmeteorologische Entscheidungsmodelle im Weinbau am Beispiel der Prognose der Rebenperonospora (Plasmopara viticola)*. Abschlußbericht AM 37, Deutscher Wetterdienst. Geisenheim, pp.75.

Huber, L. and *Gillespie, T.J.*, 1992: Modeling leaf wetness in relation to plant disease epidemiology. *Ann. Rev. Phytopathol. 30,* 53-77.

Jacobs, A.F.G., Van Pul, W.A.J., and *Van Dijken, A.*, 1990: Similarity moisture dew peofiles within a corn canopy. *J. Appl. Meteorol. 29*, 1300-1306.

Magarey, R.D., 1999: A theoretical standard for surface wetness estimation. *Ph.D. Dissertation*. Cornell University, Ithaca, NY.

Maracchi, G., 2003: *Meteorologia e Climatologia applicate* (a cura di). L'Universo, Istituto Geografico Militare, Firenze, Italy.

Orlandini, S. and *Rosa, M.*, 1997: A model for the simulation of grapevine downy mildew. *Petria 7*, Suppl. 1, 47-54.

Penrose, L.J. and *Nicol, H.J.*, 1996: Aspects of microclimate variation within apple tree canopies and between sites in relation to potential *Venturia inequalis* infections. *New Zeal. J. Crop Hort. 24*, 259-266.

Potratz, K.J., Gleason, M.L., Hockmuth, M.L., Parker, S.K., and *Pearston, G.A.*, 1994: Testing the accuracy and precision of wetness sensors in a tomato field and turfgrass. *Journal of Iowa Academic Science 101*, 56-60.

Rosa, M. and *Orlandini, S.*, 1997: Structure and application of the PLASMO model for the control of grapevine downy mildew. *Petria 7*, Suppl. 1, 61-70.

Russo, J.M., 2000: Weather forecasting for IPM. In *Emerging Technologies for Integrated Pest Management: Concepts, Research, and Implementation* (eds.: *G.G. Kennedy* and *T.B Sutton*). APS Press, St. Paul.

Seem, R.C., Magarey, R.D., Zack, J.W., and *Russo, J.M.*, 2000: Estimating disease risk at the whole plant level with general circulation models. *Environ. Pollut. 108*, 389-395.

Weiss, A. and *Lukens, D.L.*, 1981: Electronic circuit for detecting leaf wetness and comparison of wwo sensors. *Plant Disease 65*, 41-43.

Wilks, D.S., 1995: *Statistical Methods in the Atmospheric Sciences*. Academic Press, San Diego, CA.

IDŐJÁRÁS

Quarterly Journal of the Hungarian Meteorological Service
Vol. 108, No. 4, October–December 2004, pp. 265–281

Periodicity of the annual precipitation totals in Serbia and Montenegro

Ivana Tošić and **Miroslava Unkašević**

Institute of Meteorology, University of Belgrade,
P.O. Box 368, 11000 Belgrade, Serbia and Montenegro
E-mail: itosic@afrodita.rcub.bg.ac.yu

(Manuscript received February 18, 2004; in final form August 6, 2004)

Abstract—Annual precipitation totals of 13 stations in different parts of Serbia and Montenegro are analyzed for homogeneity, trend, and periodicities. The data cover time periods ranging from 50 to 70 years. Autocorrelation spectral analysis (ASA) and multitaper method (MTM) are used to investigate the periodicity of precipitation series. Spectral analysis shows peaks at frequencies corresponding to the following time periods: about 2.5–5, 8, and 14–23.3 years. Statistical significance of these peaks is discussed. These results are compared with those of other authors.

Key-words: periodicity, spectral analysis, annual precipitation series.

1. Introduction

Precipitation is one of the key elements that characterize the climate of a region. It is essential to regional water resources, agriculture, and ecosystem environment. Identifying and understanding short timescale precipitation variations is crucial for understanding regional climate variations.

Many authors analyzed the periodicities of annual precipitation in different parts of the world. *Tyson et al.* (1975) found cycles in the South African rainfall data with period ranges of 16–20 years, 3–4 years, and approximately 2 years. *Rodhe* and *Virji* (1976), in their analysis of East African rainfall data, detected spectral peaks at 2–2.5 years, 3.5 years, and 5–5.5 years. *Kousky* and *Chu* (1978), analyzing rainfall series in two large sectors of Northeast Brazil, identified prevalence of spectral peaks with periods of 2–3 years, 3–5 years, and 10–20 years. Also, *Chu* (1984) found

relative maxima of power in the frequency bands of 12.7–14.9, 4.5–4.9, and 2.4 years. A study for Central Europe indicates that short and medium periods with lengths of 2–5 years and 10–16 years appear significant (*Brázdil et al.*, 1985). Over Northern Europe there exists a 16-year cycle, in the southern part of Central Europe there is a longer cycle of 20–22 years, while periods of about 6–7 years (short term) and 10–12 years (medium terms) are evident over much of the continent (*Camuffo*, 1984; *Vines*, 1985).

The present study, motivated by earlier investigations linking regional rainfall anomalies to large-scale circulation, uses time series analysis to identify the dominant bands of these variations.

2. Data used

The basic data consists of annual rainfall totals from 13 stations in Serbia and Montenegro. The stations are shown in *Fig. 1* and listed in *Table 1*. The grouping of stations were done (*Table 1*) subjectively, but using similarities of climatic regimes: Vojvodina lowland and Belgrade, mountainous part of Serbia, and seaside of Montenegro.

Fig. 1. Location of meteorological stations listed in Table 1.

Vojvodina and Serbia have continental climates. The continental regime is characterized by maximum rainfall during summer, especially in June, with a secondary maximum in October, and by minimum precipitation during winter

(in February). Stations at the seaside of Montenegro are under the effect Mediterranean climate. The precipitation regime is controlled mainly by the subtropical Azores anticyclone in summer and the cyclonic circulation over the Tyrrhenian Sea during autumn. Therefore, the minimum precipitation appears in summer, while the maximum is during late autumn. The coast of Montenegro is influenced by the vicinity of littoral chains that exceeds the altitude of 1000 m. These chains enhance the rainfall when moist air is advected from south due to their forced uplift, causing the European maximum (4926 mm/year) of annual precipitation totals (*Ranković et al.* 1981).

Table 1. List of rainfall stations with their latitudes, longitudes, altitudes, and the lengths of available records

Regions and stations	Latitude	Longitude	Altitude (m)	Period
Lowland				
Senta	45°56'	20°05'	80	1926–1995
Kikinda	45°51'	20°28'	81	1926–1995
Zrenjanin	45°24'	20°21'	80	1926–1995
Vršac	45°09'	21°19'	84	1926–1995
Sremska Mitrovica	44°58'	19°38'	81	1926–1995
Belgrade	44°48'	20°28'	132	1926–1995
Mountainous Serbia				
Požega	43°50'	20°02'	310	1926–1995
Kraljevo	43°44'	20°41'	219	1926–1995
Dimitrovgrad	43°01'	22°45'	450	1926–1995
Vranje	42°29'	21°54'	432	1926–1995
Prizren	42°13'	20°44'	402	1926–1995
Coastal Montenegro				
Herceg-Novi	42°27'	18°33'	10	1951–2000
Bar	42°06'	19°06'	4	1951–2000

2.1 Homogeneity

The relative homogeneity of the series was tested according to *Alexandersson* (1986). The standard normal homogeneity test for the precipitation is based on the assumption that the ratio of values at the station being tested (test station) to values of a neighboring station (reference station) is fairly constant in time. The number of reference stations should be large enough to mask any eventual non-homogeneities in the reference data. The appropriate number of reference stations depends on the station network density and data quality. The central idea was to use the reference stations that are best correlated with the test station.

A test parameter T is computed for each of the $N-1$ possible change points in the time series:

$$T(m) = a\overline{P}_1^2 + (N-m)\overline{P}_2^2, \quad a = 1,2,...,N-1, \tag{1}$$

where $\overline{P}_1$ is the mean value of P during the m first years, and $\overline{P}_2$ is the mean value during the $(N-m)$ last years. The value of m is the year most probable for break. The maximum T value in the time series is denoted by T_x:

$$T_x = \max\{T(m)\}, \quad m = 1,2,...,N-1. \tag{2}$$

The critical T values for the 5% significance level (T_{95}) are 8.80 for $N = 70$, and 8.45 for $N = 50$ (*Alexandersson*, 1986). Inhomogeneity was assumed to occur in the year for which T reached its maximum value T_x. The exact year for the break was decided by station history.

In our testing of 13 precipitation series, 12 were found to be homogenous, while series of Prizren (*Fig. 2*) becomes homogeneous after being adjusted by multiplying values of the period before the inhomogeneity with an adjustment factor.

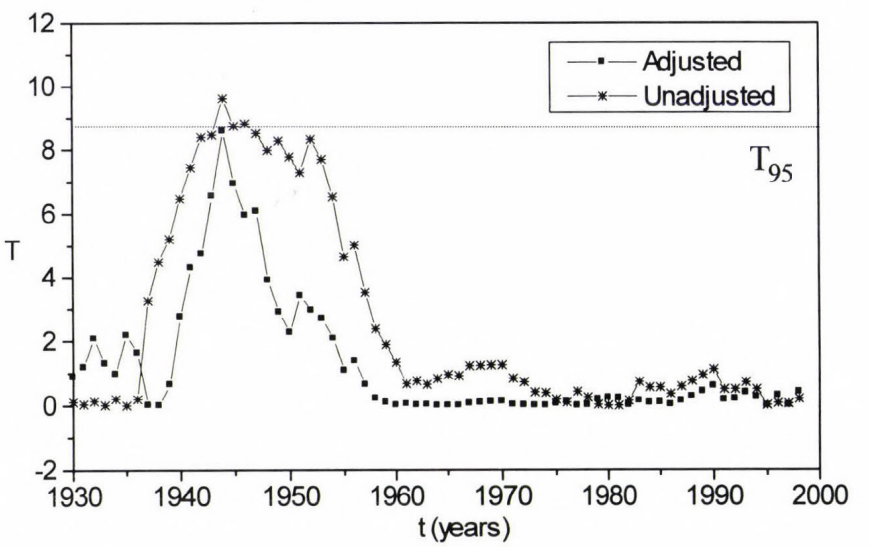

Fig. 2. Results of performing the SNHT on the annual precipitation totals for Prizren.

2.2 Trend

The presence or absence of trend in individual rainfall series have been determined using the Mann-Kendall rank statistic τ (*Kendall* and *Stuart*, 1961). This is defined as:

$$\tau = \frac{4\sum n_i}{N(N-1)} - 1, \tag{3}$$

where n_i is the number of values larger than the ith value in the series subsequent to its position in the series of N values. To apply this statistic to evaluate significance, a comparison is made with:

$$(\tau)_t = \pm t_g \sqrt{\frac{4N+10}{9N(N-1)}}, \tag{4}$$

where t_g is the desired probability point of the standard Gaussian distribution for a two sided test. Linear trend has been determined by conventional least squares regression analysis. In both types of trend evaluation, the 5% level of significance has been taken for the rejection of the null hypothesis of no trend for individual sets of data. For all stations, except for both stations at coastal Montenegro, τ lies within the range $-(\tau)_t$ and $+(\tau)_t$, so the sequence of annual precipitation totals should be assumed random.

To understand the nature of trend, and in order to remove high frequency oscillations, the series were subjected to a low-pass filter. *Hu et al.* (1998) assigned different weights to each of the 11-years in the moving average: 1/24, 1/24, 1/12, 1/8, 1/8, 1/6, 1/8, 1/8, 1/12, 1/24, and 1/24. This removes variations with periods shorter than 10 years in the time series, and retains variations of inter-decadal time scales. The symmetry of the weight distribution guarantees no phase shift of the variations in the time series after the filter is applied. *Fig. 3* shows annual precipitation, moving average, and slopes corresponding to linear trend. Stations in Vojvodina and Montenegro (significant at the 5% level) show negative trends, while stations at the mountain regions of Serbia show positive trends.

According to *Schönwiese* and *Rapp* (1997), there have been marked increases in precipitation in the latter part of the 20th century over Northern Europe with a general decrease southward to the Mediterranean. Hence, our results agree with results obtained by *Schönwiese* and *Rapp* (1997). Dry wintertime conditions over Southern Europe and the Mediterranean and wetter than normal conditions over many parts of Northern Europe and Scandinavia

are linked to strong positive values of the North Atlantic Oscillation (NAO), with more anticyclonic conditions over Southern Europe and stronger westerlies over Northern Europe (*IPCC*, 2001).

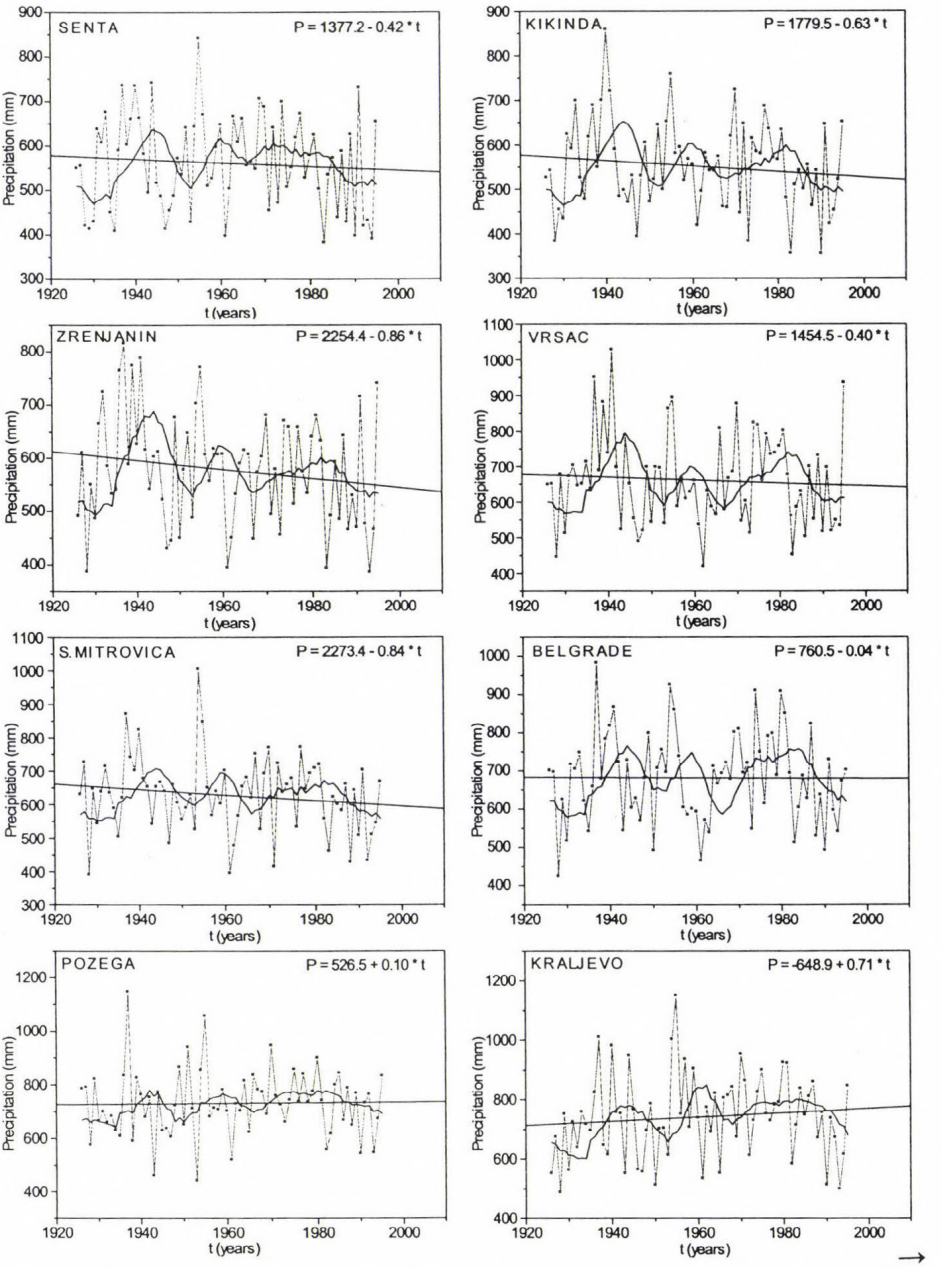

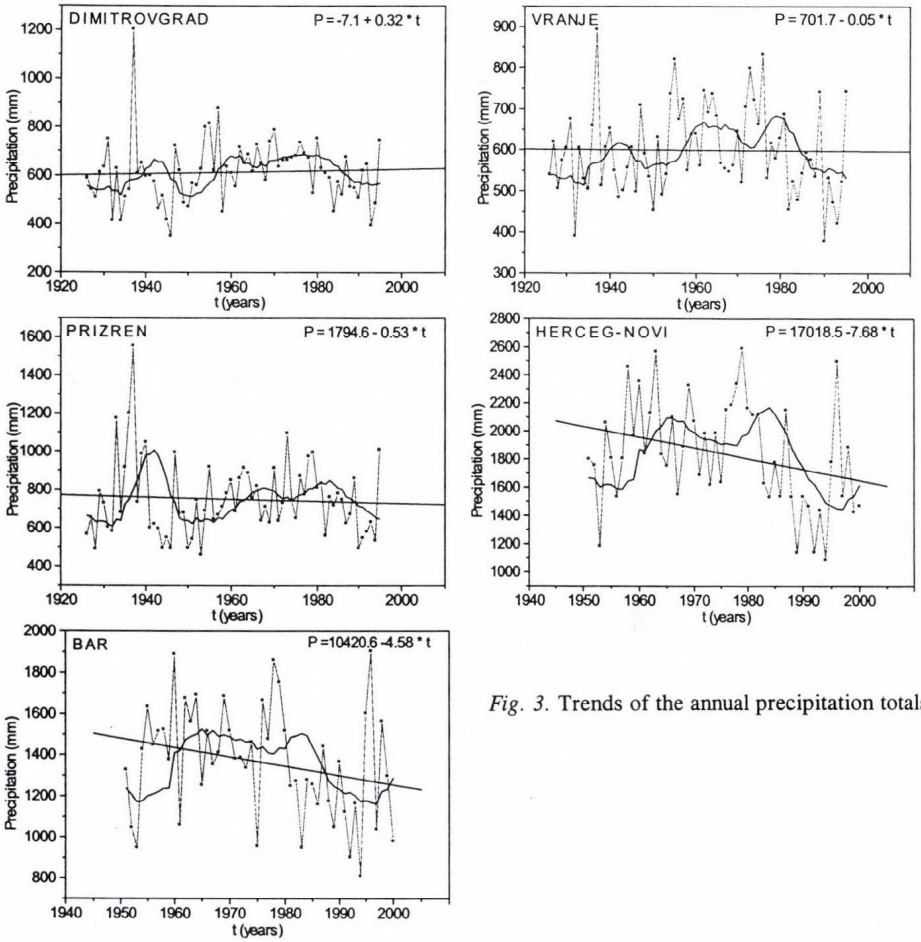

Fig. 3. Trends of the annual precipitation totals.

3. *Spectral analysis*

3.1 Methodology

Spectral analysis of discrete meteorological data sequences plays an important role in data analysis, interpretation, and searches for periodicities. Time series analysis methods aim to examine temporal sequences of data in terms of its frequency content. Various methods for estimating the spectral density function are used. In this study the power spectra of annual standardized anomalies were analyzed using the autocorrelation spectral analysis (ASA) (*Blackman* and *Tukey*, 1958; *Mitchell et al.*, 1966) and the multitaper method (MTM) (*Thompson*, 1982; *Park et al.*, 1987). The ASA is obtained by applying the discrete Fourier transform (DFT) algorithm to the correlation functions

estimated from time series, and taking the classical Hamming window as smoothing function. The averaging operation of raw spectral estimate is necessary in order to obtain a consistent estimate of the spectrum in terms of discrete estimates. In order to determine the significant peaks in the calculated spectra, the theoretical curve (null continuum) along with its associated 95% confidence level has been fitted as described by *Mitchell et al.* (1966).

Following *Tukey* (1950), the ratio between the spectral estimate and the null continuum ("white" or Markov "red noise") for any spectral component follows a Chi-square distribution (χ^2) divided by the degrees of freedom

$$\nu = \frac{2N - \frac{m}{2}}{m}, \tag{5}$$

where N is the record length analyzed, and m is the maximum lag considered in the computation of the correlation function. Thus, if we fix a confidence limit of, e.g., 95%, and compute the probability point for the χ^2 distribution at this percentage, the empirical spectral component will be significant if the ratio of the power associated with a peak in the spectrum to the local power level of the null continuum is greater than this probability point. In our case a maximum lag of $m = N/2$ is considered with a degree of freedom of 3.5, and thus a probability point close to 2.5 is used.

One of the more sophisticated methods is the MTM approach using multiple orthogonal data tapers to describe structures in time series. The statistical information discarded by the first taper is partially recovered by the second taper, the information discarded by the first two tapers is partially retrieved by the third, and so on. Only a few low-order tapers may be employed, as the spectral leakage increases with increasing order. For a given time series $x(t)$, we determine a set of S orthogonal Slepian data tapers (*Slepian*, 1978) $a_s(t)$, and their S associated tapered Fourier transforms or eigenspectra $Y_s(f)$, $s = 1,...,S$, as:

$$Y_s(f) = \sum_{t=1}^{N} a_s(t)x(t)e^{-i2\pi f t\Delta t}, \tag{6}$$

where Δt is the sampling interval.

The multi-taper spectral estimate can provide a description of an irregular oscillatory signal centered at a particular frequency f, since it can describe a variety of amplitude and phase modulations using a suitable linear combination of the S independent eigenspectra. The independent eigenspectra can be combined through a weighted average as follows:

$$\bar{Y}(f) = \frac{\sum_{s=1}^{S} \lambda_s |Y_s(f)|^2}{\sum_{s=1}^{S} \lambda_s}, \tag{7}$$

where the eigenvalues λ_s come from the eigendecomposition. The linear combination of eigenspectra given by $\bar{Y}(f)$ provides a power spectrum with optimal trade-off properties between spectral resolution and variance (*Thompson*, 1982; *Park et al.*, 1987). According to *Park et al.* (1987), only the first $K = 2p$ (p is the time-frequency bandwidth parameter) are known to have the best spectral properties, as their leakage fractions are very close to zero.

The significance of periodic signals or quasi-periodic signals was measured with respect to the noise background. The confidence levels of the noise estimate are calculated by assuming that the spectrum has a χ^2_ν distribution with $\nu \approx 2K$ degree of freedom (*Mann* and *Lees*, 1996). The ratio of the power associated with a peak in the spectrum to the local power level of the background is assumed to be distributed as χ^2/ν, and can be compared to the tabulated χ^2 probability distributions to determine peak significance.

3.2 Analysis of the results

Figs. 4 and *5* show results of the annual anomalies obtained by using ASA and MTM, respectively. There is a general agreement between the two spectral methods for shapes of power spectra. However, there are some differences in their power of spectral resolution and signal detectability. In the case of Prizren and Herceg-Novi, the lag-one autocorrelation coefficients differ significantly from zero. The annual precipitation variance spectra in these two cases can be fitted by Markov "red noise" continuum. For the other stations it should be assumed that the "null" continuum is "white noise", since the lag-one autocorrelation coefficients do not differ significantly from zero. With respect to the significant spectral peaks summarized in *Table 2*, an interesting feature is the absence of peaks with spectral density exceeding the 95% confidence level for the "null" continuum for Dimitrovgrad. Spectral analysis shows that the peaks occur mainly within the following three spectral regions: about 2–5, 8, and 14–23.3 years. The quasi-biennial oscillations (QBO) appear at Požega (2.5 years), Prizren (2.0 years), and Herceg-Novi (2.8 years). *Maheras et al.* (1992) and *Gajić-Čapka* (1994) detected the QBO periodicity when studying annual rainfall in the central Mediterranean and Croatia, respectively. *Brázdil* and *Zolotokrylin* (1995) found the QBO in monthly precipitation fields over Europe. *Lana* and *Burgueño* (2000) detected periodicities greater than 2 years in the monthly and spring analysis of rainfall anomalies for Barcelona.

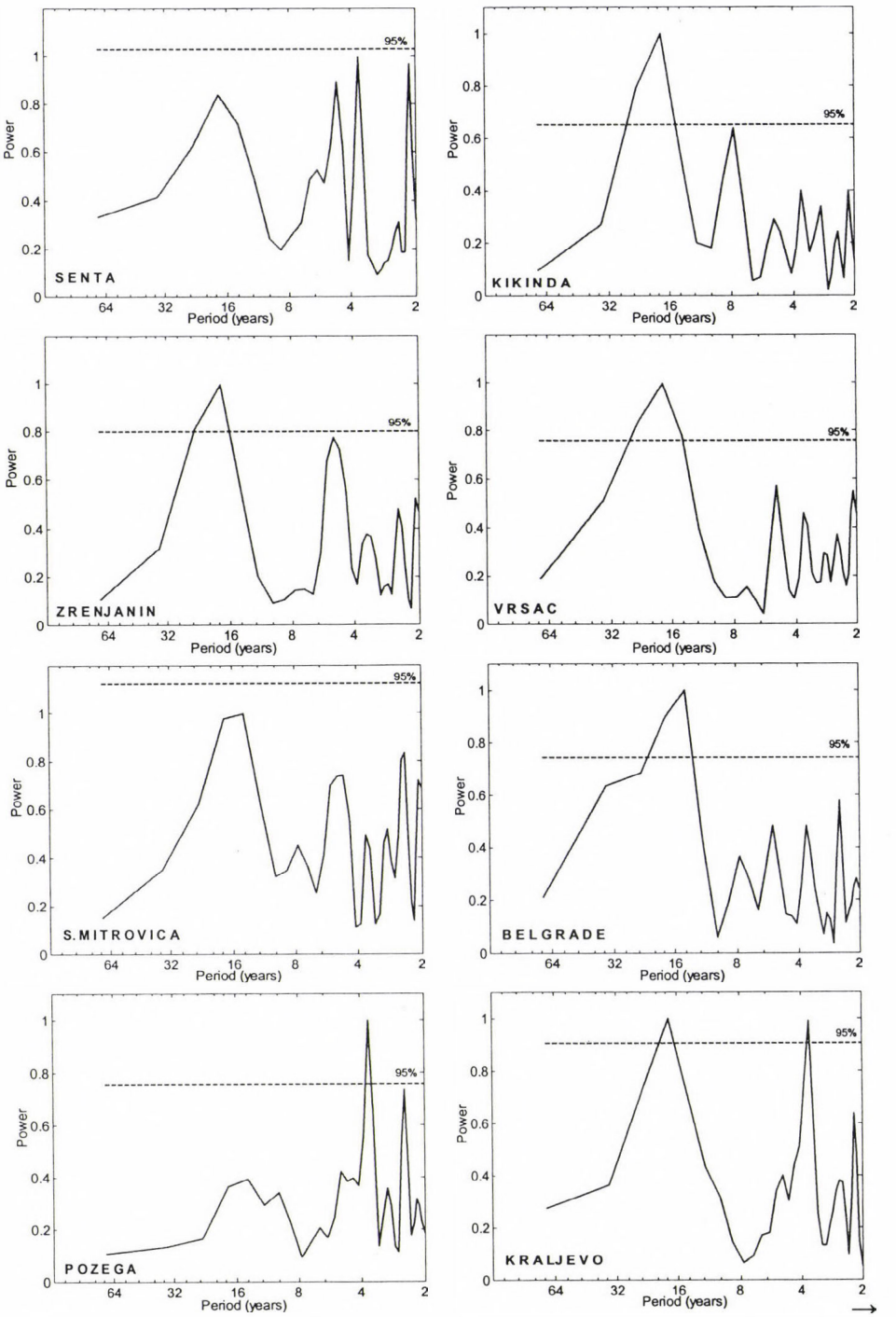
SENTA
KIKINDA
ZRENJANIN
VRSAC
S.MITROVICA
BELGRADE
POZEGA
KRALJEVO
95%
Power
Period (years)
64
32
16
8
4
2
0
0.2
0.4
0.6
0.8
1

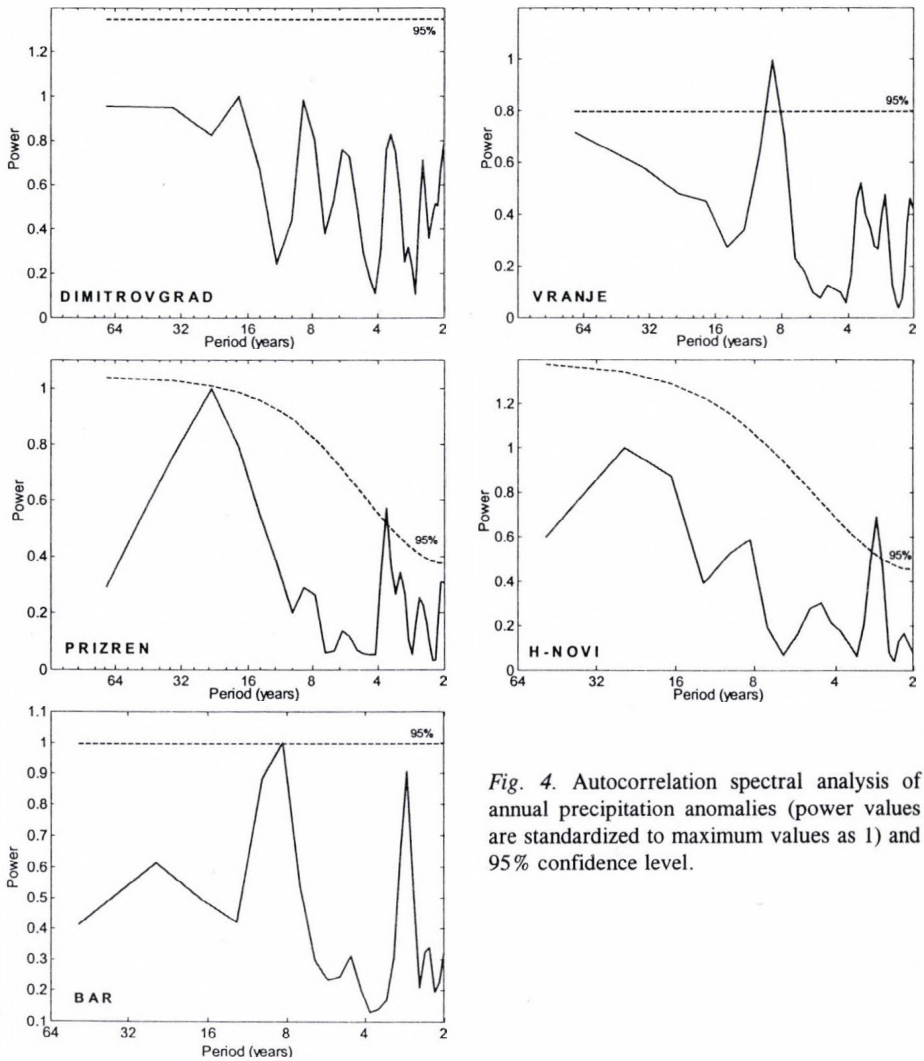

Fig. 4. Autocorrelation spectral analysis of annual precipitation anomalies (power values are standardized to maximum values as 1) and 95% confidence level.

A period of 3.7 years is common for the mountainous part of Serbia: Kraljevo, Požega, and Prizren (*Figs. 4* and *5*). *Brázdil* (1986) found statistically significant cycles in the length of 3.3–3.6 years in Central Europe (Moravia: 3.3 years, Vienna, Poland, Slovakia, Hungary: 3.6 years). *Gajić-Čapka* (1994) detected the periods of 3.6 and 3.7 years for three different climate regions of Croatia. According to *Burroughs* (1992), periodicities in the range of 3–4 and 6 years can be interpreted as higher harmonics of the sunspot cycle. Oscillation of 4.9 years is characteristic for Senta, Sremska Mitrovica, and Zrenjanin annual rainfall anomalies in Vojvodina lowland.

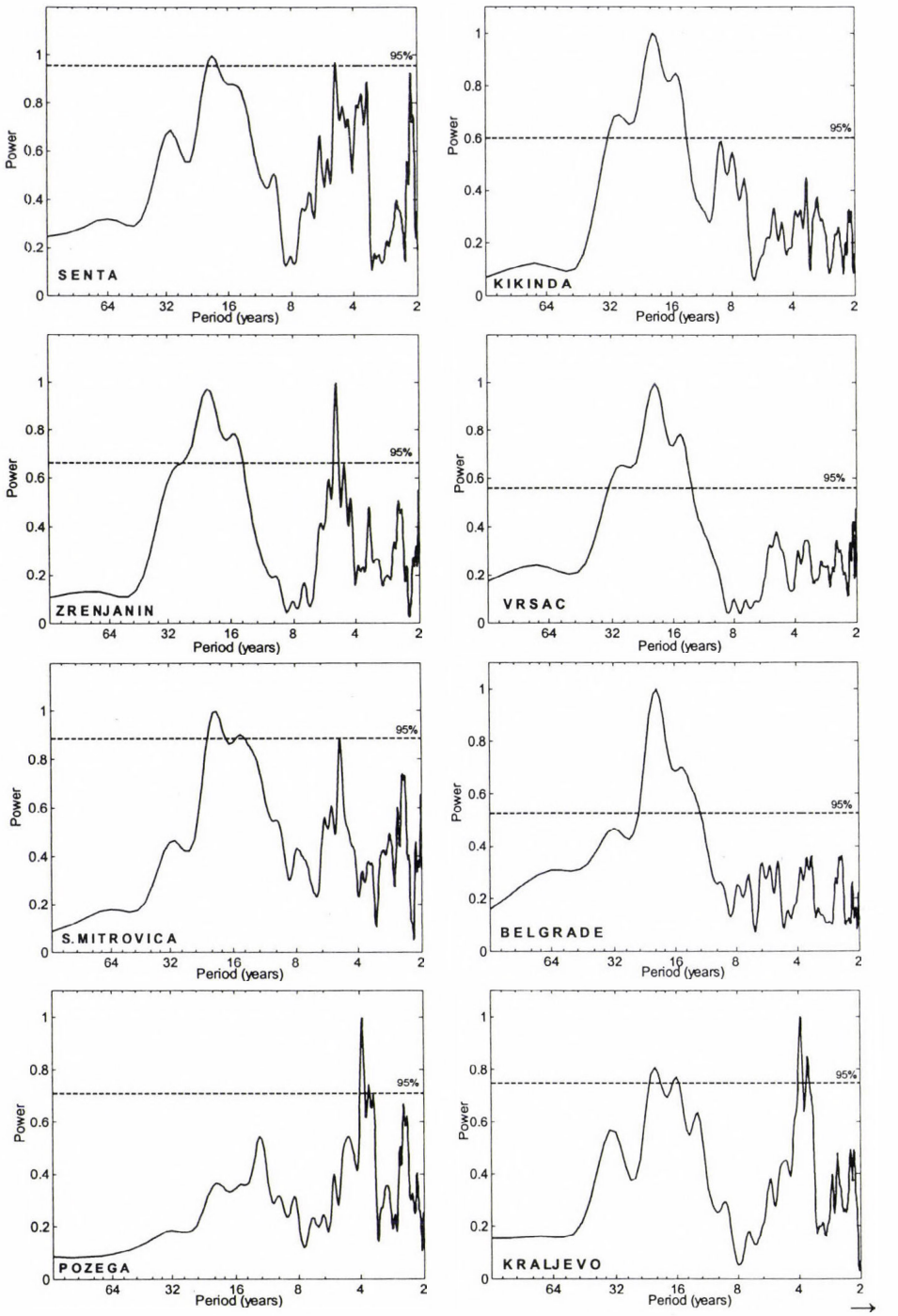
SENTA
KIKINDA
ZRENJANIN
VRSAC
S.MITROVICA
BELGRADE
POZEGA
KRALJEVO
Power
Period (years)
95%
64
32
16
8
4
2
0
0.2
0.4
0.6
0.8
1

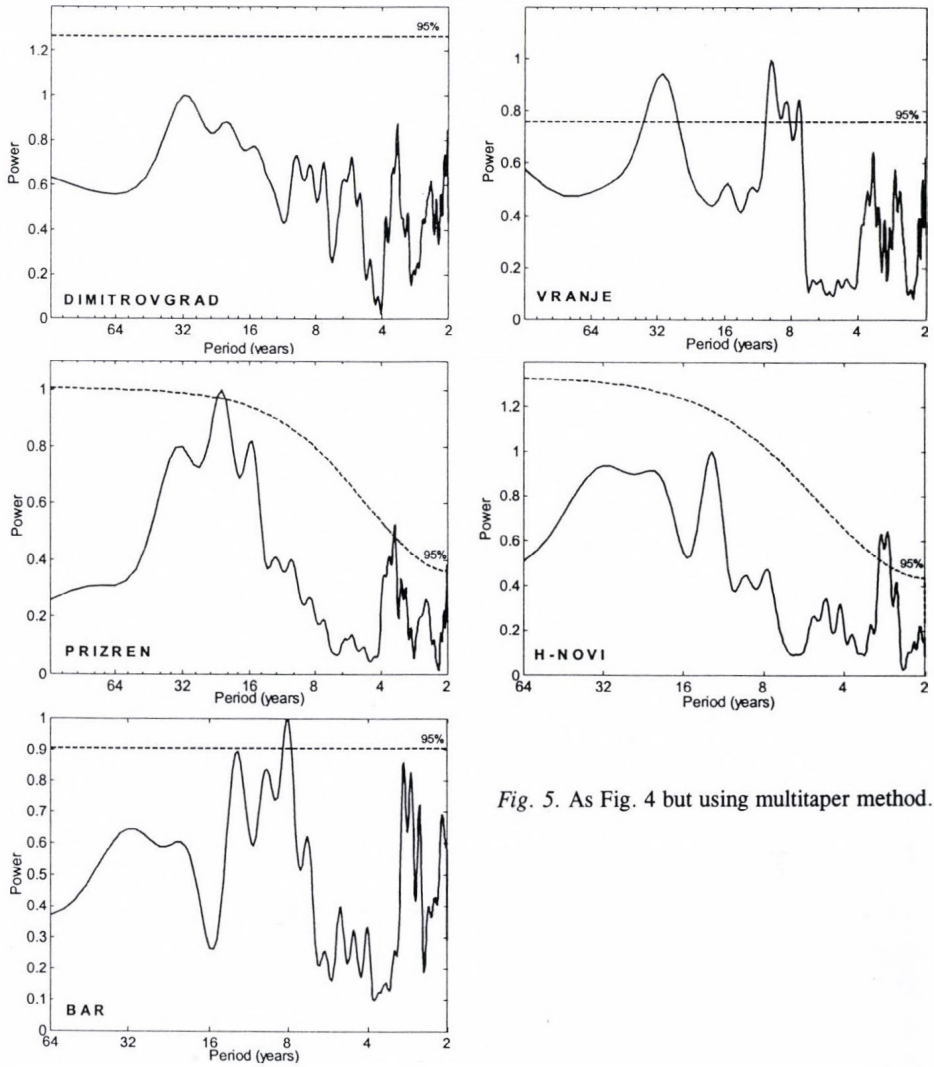

Fig. 5. As Fig. 4 but using multitaper method.

Cycle of about 8 years is detected in the analysis of the precipitation series for Bar (8.3), Kikinda (7.8), and Vranje (8.7). A seven-year period has been reported by several other authors studying different series in the Northern Hemisphere, mainly in Europe, North America, and the North Atlantic Ocean, suggesting that it may be associated with the dynamics of the atmosphere interacting with the North Atlantic Ocean. For example, *Plaut et al.* (1995) and *Banner* (1999) found a cycle of 7.7 years in the Central England temperature time series, *Moron et al.* (1998) found a cycle of 7.5 years in

North Atlantic sea surface temperatures and winter North Atlantic Oscillation Index (NAOI), *Dettinger et al.* (1995) found a cycle of 7.4 years in the United States surface air temperature records.

Table 2. Significant cycles of annual precipitation anomalies according to the 95% confidence level of the power spectra

	2	3	5	8	14	18	23.3
Senta	-	-	4.9	-	-	18.9	-
Kikinda	-	-	-	7.8	-	17.5	23.3
Zrenjanin	-	-	4.9	-	14.0	17.5	23.3
Vršac	-	-	-	-	14.0	17.5	23.3
Sremska Mitrovica	-	-	4.9	-	14.6	17.5	-
Belgrade	-	-	-	-	14.0	17.5	-
Požega	2.5	3.7	-	-	-	-	-
Kraljevo	-	3.7	-	-	-	17.5	-
Dimitrovgrad	-	-	-	-	-	-	-
Vranje	-	-	-	8.7	-	-	-
Prizren	2.0	3.7	-	-	-	-	23.3
Herceg-Novi	2.8	-	-	-	-	-	-
Bar	-	-	-	8.3	12.5	-	-

Oscillation corresponding to medium periods of about 14–23.3 years is a feature of Vršac (14–23.3), Zrenjanin (14–23.3), Kikinda (17.5–23.3), Belgrade (14–17.5), Sremska Mitrovica (14.6–17.5), Senta (18.9), Kraljevo (17.5), and Prizren (23.3). *Vines* (1985) found a cycle of 20–22 years over the southern part of Central Europe and a cycle of about 16 years for the northern part. *Maheras* and *Vafiadis* (1991) found a periodicity close to 22 years by studying annual and spring rainfalls. The double sunspot cycle has been also detected by *Rodríguez et al.* (1999) analyzing monthly series and by *Lana* and *Burgueño* (2000) in the monthly and summer rainfall anomalies for Barcelona. *Tošić* and *Unkašević* (2004) noted an oscillation of 13.3–16 years in the annual and winter precipitation series in Belgrade during the period 1889–2000.

Similarity between our spectral peaks and those for the European studies, cited above, suggests that possibly a feature of the large scale circulation pattern may be responsible for the observed fluctuations. One of the possibilities is a teleconnection with the North Atlantic Oscillation expressed by NAO Index (NAOI) (*Hurrel*, 1995). It is defined as normalized pressure difference between Ponta Delgrada (or Gibraltar) and Reykjavik. *Table 3* shows the correlation between precipitation series and NAOI. All stations

except for Sremska Mitrovica show significant negative correlation with NAO. *Reljin et al.* (2002) found significant influence of the NAO to the climate in Yugoslavia through several linear and non-linear methods of analysis.

Table 3. Correlation coefficient between the North Atlantic Oscillation and annual precipitation series

Stations	NAOI
Senta	-0.4402 **
Kikinda	-0.4336 **
Zrenjanin	-0.4000 **
Vršac	-0.3745 **
Sremska Mitrovica	-0.1949
Belgrade	-0.3323 **
Požega	-0.3723 **
Kraljevo	-0.3493 **
Dimitrovgrad	-0.2539 *
Vranje	-0.2772 *
Prizren	-0.2855 *
Herceg-Novi	-0.4075 **
Bar	-0.4218 **

* significant at 95% confidence level
** significant at 99% confidence level

4. Conclusions

Annual precipitation totals of 13 stations in different parts of Serbia and Montenegro were analyzed for homogeneity, trend, and periodicities. The normalized annual precipitation series reveal significant negative trend at 95% confidence level for coastal Montenegro series, non-significant negative trend for Vojvodina, and non-significant positive trend for mountainous Serbia.

Quasi-biennial (about 2.5 years) and quasi-triennial (3.7 years) oscillations, as well as oscillation with medium periods (14–23.3 years) found over Serbia and Montenegro are consistent with the quasi-periodic oscillation reported in other studies on fluctuations of European annual precipitation. The 7-year period, reported by several authors studying different series in the Northern Hemisphere, mainly in Europe, North America, and the North Atlantic Ocean, has been identified in this study, too. The large scale circulation pattern may be responsible for the observed fluctuations. Strong influence of a large-scale phenomenon, the North Atlantic Oscillation, on the precipitation series in Serbia and Montenegro was found.

References

Alexandersson, H., 1986: A homogeneity test applied to precipitation data. *J. Climatol. 6*, 661-675.

Banner, T.C., 1999: Central England temperatures: long-term variability and teleconnections. *Int. J. Climatol. 19*, 391-403.

Blackman, R.B. and *Tukey, J.W.*, 1958: *The Measurement of Power Spectra*. Dover Publications, New York.

Brázdil, R., 1986: *Variation of Atmospheric Precipitation in the CSSR with Respect to Precipitation Changes in the European Region*. Folia Fac. Sci. Nat. Univ. Purk Brun, Geographia 22, Brno.

Brázdil, R. and *Zolotokrylin, A.N.*, 1995: The QBO signal in monthly precipitation fields over Europe. *Theor. Appl. Climatol. 51*, 3-12.

Brázdil, R., Šamaj, F., and *Valovič, Š.*, 1985: Variation of spatial annual precipitation sums in Central Europe in the period 1881-1980. *J. Climatol. 5*, 617-631.

Burroughs, W.J., 1992: *Weather Cycles, Real or Imaginary*? Cambridge University Press, Cambridge, 201 pp.

Camuffo, D., 1984: Analysis of the series of precipitation at Padova, Italy. *Climatic Change 6*, 57-77.

Chu, P.S., 1984: Time and space variability of rainfall and surface circulation in the northeast Brazil-tropical Atlantic sector. *J. Meteorol. Soc. Japan 26*, 363-369.

Dettinger, M.D., Ghil, M., Strong, C.M., Weibel, C.M., and *Yiou, P.*, 1995: Software expedities singular-spectrum analysis of noisy time series. Eos, Trans. American Geophysical Union *76*(2), 12-21.

Gajić-Čapka, M., 1994: Periodicity of annual precipitation in different climate regions of Croatia. *Theor. Appl. Climatol. 49*, 213-216.

Hu, Q., Woodruff, C.M., and *Mudrick, S.E.*, 1998: Interdecadal variations of annual precipitation in the Central United States. *B. Am. Meteor. Soc. 79*, 221-229.

Hurrel, J.W., 1995: Decadal trends in the North Atlantic Oscillation regional temperatures and precipitation. *Science 269*, 676-679.

IPCC, 2001: *Climate Change 2001: The Scientific Basis*. Cambridge University Press, Cambridge, 881 pp.

Kendall, M.G. and *Stuart, A.*, 1961: *The Advanced Theory of Statistics 2*. Charles Griffen, 483-484.

Kousky, V.E. and *Chu, P.S.*, 1978: Fluctuations in annual rainfall for Northeast Brazil. *J. Meteorol. Soc. Japan 56*, 457-465.

Lana, X. and *Burgueño, A.*, 2000: Statistical distribution and spectral analysis of rainfall anomalies for Barcelona (NE Spain). *Theor. Appl. Climatol. 66*, 211-227.

Maheras, P. and *Vafiadis, M.*, 1991: Fluctuations temporelles des precipitations à Sofia et à Thessaloniki durant la dernière pèriode seculaire. *Societa Geogr. Italiana XVI*, 543-553.

Maheras, P., Balafoutis, C., and *Vafiadis, M.*, 1992: Precipitation in the central Mediterranean during the last century. *Theor. Appl. Climatol. 45*, 209-216.

Mann, M.E. and *Lees, J.M.*, 1996: Robust estimation of background noise and signal detection in climatic time series. *Climatic Change 33*, 409-445.

Mitchell, J.M. et al., 1966: Climatic change. *WMO Tech. Note 79*. WMO No. 179, Geneva, 79 pp.

Moron, V., Vautard, R., and *Ghil, M.*, 1998: Trends, interdecadal and interannual oscillations in global sea-surface temperatures. *Clim. Dynam. 14*, 545-569.

Park, J., Lindberg, C.,. and *Vernon, F.L.*, 1987: Multitaper spectral analysis of high-frequency seismograms. *J. Geophys. Res. 92*, 12675-12684.

Plaut, G.R., Ghil, M., and *Vautard, R.*, 1995: Interannual and interdecadal variability in 335 years of central England temperature. *Science 268*, 710-713.

Ranković, S., Radičević, D. and *Sokolović-Ilić, G.*, 1981: Basic characteristics of the precipitation distribution in Yugoslavia - Contribution to the maps of *Climate Atlas, Note 2*. Federal Hydrometeorological Institute of Yugoslavia, Belgrade, Yugoslavia, 226 pp.

Reljin, I., Jovanović, G., and *Reljin, B.*, 2002: The analyses of FRY climate and NAO teleconnection. *Proc. Conf. on Information Technologies-Present and Future*, IT '02 Zabljak, 33-37.

Rodhe, H. and *Virji, H.*, 1976: Trends and periodicities in East African rainfall data. *Mon. Weather Rev. 104*, 307-315.

Rodríguez, R., Llasat, M.C., and *Wheeler, D.*, 1999: Analysis of the Barcelona precipitation series 1850-1991. *Int. J. Climatol. 19*, 787-801.

Schönwiese, C.D. and *Rapp, J.*, 1997: *Climate Trend Atlas of Europe Based on Observations 1891-1990.* Kluwer Academic Publisher, Dodrecht, 228 pp.

Slepian, D., 1987: Prolate spheroidal wave function, Fourier anaysis and uncertainty, V. The discrete case. *AT&T Tech. J. 57*, 1371-1429.

Thomson, D.J., 1982: Spectrum estimation and harmonic analysis. *Proc. IEEE 70*, 1055-1096.

Tošić, I. and *Unkašević, M.*, 2004: Analysis of precipitation series for Belgrade. *Theor. Appl. Climatol.* (in press).

Tukey, J.W., 1950: The sampling theory of power spectrum estimates. *Symp. on Applications of Autocorrelation Analysis to Physical Problems*. US Office of Naval Research. NAVEX-P-735 47-67, Washington D.C.

Tyson, P.D., Dyer, T.G., and *Mametse, M.N.*, 1975: Secular changes in South African rainfall: 1880 to 1972. *Q. J. Roy. Meteor. Soc. 101*, 817-833.

Vines, R.G., 1985: European rainfall patterns. *J. Climatol. 5*, 607-616.

NEWS

The EMS Young Scientist Award winner in 2004

The European Meteorological Society (EMS) Awards Committee conferred the "Young Scientist Award" on a Hungarian scientist, *Szilvia Horváth* in Nice, France, on September 27, 2004.

Supporting the aspiring young scientists is one of the central activities of the European Meteorological Society. At the first time, the Award was presented at the EMS Annual Meeting in Rome, 2003.

Young scientists from the EMS Member countries are entitled to receive this Award. According to the requirements, the candidate must have written a high quality publication published during the previous three years in a reviewed international scientific journal, or an outstanding PhD thesis. Qualification also needs a supporting statement by the EMS Member Society (in this case by the Hungarian Meteorological Society), too.

In order to support excellence among young European scientists, EMS honors each year one promising candidate with the Award. This Award includes a diploma and a sum of 1000 EUR. The winner is also invited for participation in the EMS Annual Meeting, where the Award is presented.

The year 2004 Award was conferred on the author for her PhD thesis entitled "20th century variations of the soil moisture content in East-Hungary".

The Award Ceremony took place during the opening session of the Fourth Annual Meeting of the European Meteorological Society on September 27, 2004. Participants of the Award Ceremony were addressed by *Prof. Werner Wehry*, President of the European Meteorological Society; *Prof. Susan K. Avery,* President of the American Meteorological Society, and *Dr. Arne Spekat,* Executive Secretary of the European Meteorological Society.

At the end of the ceremony, the author expressed her acknowledge to her PhD supervisors, *Dr. János Mika* (Hungarian Meteorological Service) and *Dr. László Makra* (University of Szeged, Department of Climatology and Landscape Ecology), for their advices, ideas, and non-stop co-operation; her colleagues for their support and help, her family for their patience and frequent assistance; the Hungarian Meteorological Society for the recommendation, and the EMS Awards Committee, for the idea and management of this Award.

Summary of the
EMS Young Scientist Award, 2004 winner PhD thesis

20th century variations of the soil moisture content in East-Hungary

by

Szilvia Horváth

*University of Szeged, Department of Climatology and Landscape Ecology, Szeged, Hungary**

Summary—Hungary and the eastern part of the Great Hungarian Plain have always been characterized by significant hydrological extremities. The aim of the dissertation is to give a modern climatographical analysis on the varied hydrometeorological relations of the region, based on reliable observations of meteorological stations. The analysis includes statistical characteristics of the inter-annual variability, spatial, and temporal correlation of the available soil moisture content and long-range changes, as well as their possible relation with climatic trends for greater regions, respectively. The above-mentioned aims are intended to realize on the basis of the *Palmer's Drought Severity Index* (PDSI) data series, known world-wide in the agroclimatological analysis. Monthly PDSI data series of five stations (Miskolc, Nyíregyháza, Debrecen, Kecskemét, and Szeged) were determined for the 20th century (99 years), in three versions: (*a*) plant-covered surface (maize plant) and homogenized; (*b*) bare (not plant-specific) surface, homogenized; and (*c*) plant-covered surface, but non-homogenized meteorological data. For studying the spatial correlation, PDSI sets of 17 stations were calculated for the period between 1951 and 1992. The results are as follows: place-independence of the PDSI is realized, but season-independence is only partly on the Great Hungarian Plain. By analyzing the PDSI sets of each station and month separately, the distribution of the samples can be considered normal. PDSI can correctly be interpreted as a characteristic of the soil moisture content. PDSI anomalies show regional differences and definite structures in the examined region. The high autocorrelation makes it possible to define so called year-types (dry, wet, medium) objectively. The trends for each month and station are negative. Decreasing soil moisture content is connected not only with the time, but the warming characterizing the average of the northern hemisphere, too. Significant wet sub-periods are detected in the first half of the 20th century, while dry breaks occurred in the second half of the century. The two methods for calculating the index (Thornthwaite, Blaney-Criddle) and the homogenisation of the original parameters influence the statistical characteristics of the index series only slightly.

**Present address: Ministry of Environment and Water, H-1394 Budapest, P. O. Box 351, Hungary; E-mail: horvath@mail.kvvm.hu*

Hans Ertel – a pioneer in meteorological sciences

(A brief historical review on the occassion of his 100th birthday)

In 1946 Hans Ertel was appointed professor of Geophysics at the University of Berlin, and director of the Institute of Meteorology and Geophysics. He died suddenly and unexpectedly in 1971. He was visiting professor at the University of Uppsala (Sweden) and met there his old friend, the theoretical meteorologist, Hilding Koehler as well as Markus Bath. Koehler was the tutor of Bert Bolin and contributed significantly to the scientific career of Carl-Gustaf Rossby. It is of historical interest, that Ertel and Rossby met again after the war in Stockholm and Uppsala, when Uppsala invited Ertel to give some lectures. Rossby was the first foreign guest to visit Ertel's institute in Berlin after the war. Rossby's lecture on the waves, later named after him, have shown that this concept was implicitly included in Ertel's paper but they did not became known to the Anglo-American scientific community. It is sadly true that many important papers by Hans Ertel published in the 1940s in the "Meteorologische Zeitschrift" did not get known to researchers in the United States and England due to the war.

A later publication by Ertel, co-authored by Rossby, remained similarly unknown for a period of time. This situation changed when C. Truesdall studied Ertel's papers and presented a general survey in his well-known paper in the "Handbuch der Physik".

With the re-opening of the Institute of Meteorology, Ertel started many successful projects both as university professor and researcher. His activity became even broader, when in 1948 he was appointed director of the Institute of Physical Hydrology of the German Academy of Sciences (DAW) in Berlin. In this institute he continued his hydrodynamic research and, in addition, he started to tackle, with his staff, important geoecological issues. These activities are considered today as pioneering work. The fields of research of this institute, e.g., theoretical hydrodynamics, the special hydrography of Northern German lakes and coasts (coast protection), hydraulic nomography, hydrographic cartography, and the weather history of Europe, were successfully studied by a small staff and led within a short time to a high international reputation for the institute. Many results were published in the journal of the institute, "Acta Hydrophysica", and Curt Weikinn succeeded in publishing an internationally recognized source-book on weather history. In later years Ertel was increasingly engaged in problems of coast protection in the framework of the activities of the Academy, and this research resulted in new insights in for example the theory of lake embankment, the problem of sudden increases of the sea level, as well as many new results in theoretical geomorphology. Ertel published a considerable part of his work in the "Monatsberichte der Deutschen Akademie der Wissenschaften" (Monthly Reports of the German Academy of Sciences). This journal was not very well

known internationally, and these important papers became better known only later (through, for example, Scheidegger's "Theoretical Geomorphology"). Ertel treated meteorological problems, too, as shown by his studies "Influence of the orography on the development of weather" in the framework of the Conferences on Carpathian Meteorology.

In 1949 Ertel was elected to be an ordinary member of the German Academy of Sciences in Berlin and became its vice president for ten years. During this time many new institutes of the Academy were founded, and German-German co-operation was promoted. For the latter, Ertel joined forces with Julius Bartels, especially within the framework of the International Geophysical Year. Ertel participated intensively in other international projects such as the Decade of Hydrology, and he took part in the Carpathian Co-operation. He attended many conferences and strongly influenced international co-operation in this field.

Ertel was editor of the journals Gerlands Beiträge zur Geophysik, Zeitschrift für Meteorologie, Forschungen und Fortschritte, and Deutsche Literaturzeitung, published with the co-operation of the German academies. He was in the editorial board of "Időjárás" and "Geofisica e applicata". He was also involved in the "Alexander-von Humboldt-Forschung" for which the DAW founded a special commission on his advice and published in 1959 a Humboldt memorial volume.

Ertel's later interests were partly determined by those of his institute, but he returned often to meteorological problems and worked on an extension of geophysically oriented hydrodynamics with its wide ranging applications.

Ertel considered his fields to be theoretical mechanics (thus Theoretical Mechanics was added in 1960 to the name of his university institute) and mathematical physics, and devoted himself to the task of elaborating the laws of physics in forms applicable to the Earth and Universe.

Ertel's vorticity theorems are formulated to be valid and directly applicable in all systems of reference and with many complementary conditions. They make it possible to discuss the dependence of the continuum on non-mechanical parameters, including thermodynamic parameters (such as temperature) and physical-chemical ones (such as air humidity). Thus, they enable us to deduce mathematically the excitation and annihilation of vortices. Ertel's theorems are, however, valid for all continua in which a vortex potential can be defined; thus they are also valid in magnetohydrodynamics.

The problem of the validity limits of the continuum physics and the possibility of deducing them from atomistics have been repeatedly discussed by Hans Ertel and H.-J. Treder. Ertel supposed that this problem would never be solved "in a final form". Ertel supposed a stochastic cause in atomistic variations as in the "macroscopically random" swinging over of unstable weather situations, and generally the basis of the "randomness" both in space and time of the transitions of unstable situations into stable ones.

In the 30's Ertel was known in certain circles as a cosmologist. His corresponding works were supported among others by von Laue, Einstein, and Schrödinger. Treder remarked to Ertel that all universe models, both Newtonian and Einsteinian ones together with their modifications, emerge from the fact that the Hamiltonian of the cosmos is constant. Ertel, as a potential theorist, suggested at once that this is identical with the statement that the average variations of the Newtonian gravity potential disappear in cosmic dimensions.

Selected works of Hans Ertel have recently been collected and published in a Volume of the Beitrage zur Geschichte der Geophysic und Kosmischen Physik Band VI, Heft 3, 2005, entitled Geophysical Fluid Dynamics (ed.: W. Schröder).

In the book many of Ertel's important results are contained, e.g., the Ertel-Cadez theorem for meteorology and hydrography, the Gauss-Argand diagram, the vorticity of streaming about hills, and many others.

Wilfried Schröder.
Geophysical Institute
D 28777 Bremen-Roennebeck
Germany

IDŐJÁRÁS

VOLUME 108 * 2004

BUDAPEST, HUNGARY

AUTHOR INDEX

TABLE OF CONTENTS

I. Papers

II. Book review

III. News

SUBJECT INDEX

GUIDE FOR AUTHORS OF *IDŐJÁRÁS*

The purpose of the journal is to publish papers in any field of meteorology and atmosphere related scientific areas. These may be

- research papers on new results of scientific investigations,
- critical review articles summarizing the current state of art of a certain topic,
- short contributions dealing with a particular question.

Some issues contain "News" and "Book review", therefore, such contributions are also welcome. The papers must be in American English and should be checked by a native speaker if necessary.

Authors are requested to send their manuscripts to

Editor-in Chief of IDŐJÁRÁS

P.O. Box 39, H-1675 Budapest, Hungary

in three identical printed copies including all illustrations. Papers will then be reviewed normally by two independent referees, who remain unidentified for the author(s). The Editor-in-Chief will inform the author(s) whether or not the paper is acceptable for publication, and what modifications, if any, are necessary.

Please, follow the order given below when typing manuscripts.

Title part: should consist of the title, the name(s) of the author(s), their affiliation(s) including full postal and E-mail address(es). In case of more than one author, the corresponding author must be identified.

Abstract: should contain the purpose, the applied data and methods as well as the basic conclusion(s) of the paper.

Key-words: must be included (from 5 to 10) to help to classify the topic.

Text: has to be typed in double spacing with wide margins on one side of an A4 size white paper. Use of S.I. units are expected, and the use of negative exponent is preferred to fractional sign. Mathematical formulae are expected to be as simple as possible and numbered in parentheses at the right margin.

All publications cited in the text should be presented in a *list of references*, arranged in alphabetical order. For an article: name(s) of author(s) in Italics, year, title of article, name of journal, volume, number (the latter two in Italics) and pages. E.g., *Nathan, K.K.,* 1986: A note on the relationship between photo-synthetically active radiation and cloud amount. *Időjárás 90,* 10-13. For a book: name(s) of author(s), year, title of the book (all in Italics except the year), publisher and place of publication. E.g., *Junge, C. E.,* 1963: *Air Chemistry and Radioactivity.* Academic Press, New York and London. Reference in the text should contain the name(s) of the author(s) in Italics and year of publication. E.g., in the case of one author: *Miller* (1989); in the case of two authors: *Gamov* and *Cleveland* (1973); and if there are more than two authors: *Smith et al.* (1990). If the name of the author cannot be fitted into the text: *(Miller,* 1989); etc. When referring papers published in the same year by the same author, letters a, b, c, etc. should follow the year of publication.

Tables should be marked by Arabic numbers and printed in separate sheets with their numbers and legends given below them. Avoid too lengthy or complicated tables, or tables duplicating results given in other form in the manuscript (e.g., graphs)

Figures should also be marked with Arabic numbers and printed in black and white in camera-ready form in separate sheets with their numbers and captions given below them. Good quality laser printings are preferred.

The text should be submitted both in manuscript and in electronic form, the latter on diskette or in E-mail. Use standard 3.5" MS-DOS formatted diskette or CD for this purpose. MS Word format is preferred.

Reprints: authors receive 30 reprints free of charge. Additional reprints may be ordered at the authors' expense when sending back the proofs to the Editorial Office.

More information for authors is available: antal.e@met.hu

Information on the last issues: http://omsz.met.hu/irodalom/firat_ido/ido_hu.html

Published by the Hungarian Meteorological Service

Budapest, Hungary

INDEX: 26 361

HU ISSN 0324-6329